Accurate Discrete-Time Modeling and Boundary Analysis for High-Order Wireless Power Transfer Systems

Kai He, *Student Member, IEEE*, Xin Liu, *Member, IEEE*, Fei Gao, *Member, IEEE*, Xijun Yang, *Member, IEEE*, Zhengshun Cheng, and Dong Liu, *Senior Member, IEEE*

***Abstract*—The traditional stroboscopic mapping (SM) only focuses on the behaviors in periodic time instants, which will lose the details of multiple state changes during an operating period and cannot be used to analyze the characteristics of the studied system accurately. In this article, an improved full-power SM (IFSM) model is proposed for high-order wireless power transfer (WPT) systems and dc–dc converters, which have generality and high accuracy. The dual-side *LCC* compensated WPT system for electric vehicles is taken as an example to present the derivation of the discrete-time model. Based on the proposed model, the possible zero current switching points of the system are calculated and compared for the optimal power transfer ability. The process of the boundary calculation of the output current operating in continuous conduction mode (CCM) and discontinuous conduction mode (DCM) is proposed, which aims to provide guidelines for adopting different control strategies when the battery packs are charged in different modes. It is found that the CCM/DCM boundaries are highly related to the operating frequency and equivalent resistance of the battery packs, while the coupling coefficient of coils has little influence on it. A dual-side *LCC* WPT prototype is built, and both the simulation and experimental results match well with the theoretical analysis.**

***Index Terms*—Continuous conduction mode/discontinuous conduction mode (CCM/DCM) boundary, dual-side *LCC*, electric vehicles (EVs), improved stroboscopic mapping (SM).**

Manuscript received 10 March 2024; revised 29 April 2024; accepted 17 May 2024. Date of publication 31 May 2024; date of current version 7 October 2024. This work was supported in part by the National Natural Science Foundation of China under Grant 52377194 and Grant 52307012 and in part by Shanghai Jiao Tong University Deep Blue Program under Grant SL2022MS009. Recommended for publication by Associate Editor C. Tse. *(Corresponding author: Fei Gao.)*

Kai He, Xijun Yang, and Dong Liu are with the Department of Electrical Engineering, Shanghai Jiao Tong University, Shanghai 200240, China (e-mail: hk_3823@sjtu.edu.cn; yangxijun@sjtu.edu.cn; dongliu@sjtu.edu.cn).

Xin Liu is with the Shenzhen Institute for Advanced Study, University of Electronic Science and Technology of China, Shenzhen 518110, China (e-mail: liu_xin@uestc.edu.cn).

Fei Gao is with the Laboratory of Control of Power Transmission and Conversion, Ministry of Education, Shanghai Jiao Tong University, Shanghai 200240, China, and also with the Department of Electrical Engineering, Shanghai Jiao Tong University, Shanghai 200240, China (e-mail: fei.gao@sjtu.edu.cn).

Zhengshun Cheng is with the School of Ocean and Civil Engineering, Shanghai Jiao Tong University, Shanghai 200240, China (e-mail: zhengshun.cheng@sjtu.edu.cn).

Color versions of one or more figures in this article are available at https://doi.org/10.1109/TPEL.2024.3405205.

Digital Object Identifier 10.1109/TPEL.2024.3405205

I. Introduction

With the rapid development of electric vehicles (EVs), wireless power transfer (WPT) system has attracted extensive attention of researchers due to its advantages such as safety, high reliability, and convenience. Dual-side *LCC* compensation circuit has been widely used for EV wireless chargers because of the following characteristics.

1) The resonant current of the converter is linearly related to the dc bus voltage. When the dc bus voltage increases from 400 to 800 V, the resonant current of the receiving coil and the output power can be doubled [1].
2) The two serial inductors on the primary and secondary sides can be used to adjust the output power for various operating conditions [2].
3) The compensation network can operate at a constant switching frequency, which is independent of the coupling coefficient [3].

However, the operating state of the EV charging system is not always constant. For example, the equivalent resistance of a 48 V lithium-ion battery is different in constant-current (CC) and constant-voltage (CV) charging modes, which varies from 3.2 to 241.7 Ω [4]. The EV charging system will operate in CC mode when the battery pack is to be filled [5], during this period, the equivalent impedance will increase, causing the output current of the compensation network to enter discontinuous conduction mode (DCM) operation. Besides, for the dynamic wireless EV chargers, the coupling coefficient changes as the car moves [6]. When the current enters DCM, it will cause problems such as high total harmonic distortion (THD), and fluctuations of output voltage or current [7], [8]. Consequently, the secondary side is equivalent to the ideal current source, the calculation result will deviate much from the actual result. Moreover, there is no algorithm suitable for DCM operation because of the difficulty in output voltage estimation [9], especially for high-order systems. Thus, it is necessary to get the boundary of the output current of the compensation network for adopting different control strategies. And there is little literature talking about the relationship among load resistance, operation frequency, continuous conduction mode (CCM)/DCM, etc.

For the further understanding and parameter design of dual-side *LCC* compensated WPT system, mathematical modeling is one of the most effective solutions. The dominating method is

based on mature physical laws such as Kirchhoff's law, which can well reveal the system characteristics [10]. AC impedance analysis is used to calculate the sinusoidal ac circuits [11]. However, the compensation networks in WPT systems are often connected to a dc output, which makes ac impedance analysis not applicable. Alternatively, the generalized state-space average (GSSA) can be used to model the converter behaviors [12], where the Fourier series is used to represent the state variables in the process of modeling, and the transformation from the time domain to frequency domain analysis is realized. However, many variables need to be considered under the high accuracy requirement of GSSA. Similarly, the extended describing function (EDF) [13] decomposes the signal into sine, cosine, and dc components, using the coefficients of the decomposed signal to build a mathematical model. The coupled mode theory (CMT) [14], [15] and parity-time (PT) [16], [17] symmetry have limitations due to their assumptions. The methods mentioned above suffer from low accuracy, high order, and difficulty in analytical solutions when modeling high-order systems. To reduce the switching losses, compensation converters need to operate in zero voltage switching (ZVS) or zero current switching (ZCS). Thus, it is important to find the soft-witching region of the inverter in the WPT system and achieve the ideal power transfer efficiency based on the mathematical modeling.

The application of the discrete-time modeling method to the converters can effectively simplify the calculation and achieve high accuracy. Discrete-time synchronization modeling is used to derive a small-signal model and achieve synchronization control for the series-series WPT system [18]. A discrete-time model of the distributed power systems in the time domain is presented in [19], which aims to simplify the problem caused by the interaction between the subconverters. To describe the dynamic behaviors of the *LCC*-compensated WPT systems, a discrete-time model is used to analyze the nonlinear inverter and rectifier in [20]. To design the dual-loop control for the seven-level rectifier, a discrete small-signal model is established in [21], which can accurately predict the dynamic response of the converter in a small signal. Stroboscopic mapping (SM) is proposed to analyze nonlinear dynamic phenomena in dc–dc converters [22]. However, the discrete-time models mentioned above are either complex or not accurate enough and only focus on the performance of the systems that operate in a specific operating state. Currently, little literature is concentrating on the accurate solutions of high-order WPT systems in the full-power range. And the CCM/DCM boundary in a wide load range is also poorly studied by discrete models.

Different from the traditional SM, a discrete-time improved full-power SM (IFSM) model, which has high accuracy and can be used to analyze the boundaries of high-order WPT systems without limitation of parameter selection is developed in this article. The characteristics of the CCM/DCM boundary of the *LCC-LCC* WPT system are analyzed in the full-power range.

The main contributions of this article are as follows.

1) An IFSM model, which considers the information of all state changes and is suitable for all dc–dc converters, is proposed for high-order WPT systems.

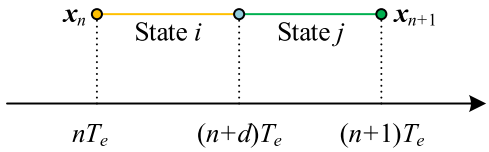

Fig. 1. Principle of discretizing time sequences in [30].

2) The possible ZCS operating frequencies of the system are calculated based on the proposed model, and the optimal one of which is selected.
3) The analysis process of the CCM/DCM boundary of the WPT system with respect to the coupling coefficient, operating frequency, and equivalent load resistance is proposed, which aims to provide guidelines for adopting different control strategies.

The rest of this article is organized as follows. Section II gives a brief review of the existing discrete-time modeling methods. The reasons why the existing methods do not apply to high-order WPT systems are explained. Section III presents the core idea and derivation of the proposed discrete-time model. Section IV presents the possible ZCS frequency calculation and selection based on the proposed model. Section V analyzes the CCM/DCM boundaries and constraints of the *LCC-LCC* WPT system. Section VI presents the experimental results. Section VII concludes this article.

II. Brief Review of the Existing Discrete-Time Modeling

In this section, the existing discrete-time modeling methods will be briefly reviewed, and the difficulties in modeling for high-order WPT systems with multiple operating states using these methods are explained.

For dc–dc systems, the state equation can be described as

$$\frac{d\boldsymbol{x}(t)}{dt} = \boldsymbol{A}_i \boldsymbol{x}(t) + \boldsymbol{B}_i \boldsymbol{u}(t) \tag{1}$$

where $\boldsymbol{A}_i$ and $\boldsymbol{B}_i$ are the state matrix and input matrix of the system in different subintervals, respectively. $\boldsymbol{x}(t)$ is the state vector, and $\boldsymbol{u}(t)$ is the input voltage vector.

A. Existing Discrete-Time Modeling Methods

1) Small-Step Discretization Method: As shown in Fig. 1, a small-time interval T_e is defined to discretize the continuous time sequence in [30], the operating state only changes once in one-time interval. Then, the state variables between the *i*th and *j*th operating states of the system are calculated by the Euler method, which is

$$\begin{aligned}\boldsymbol{x}_{e|n+1} =& \left(\boldsymbol{A}_j\left(\left(\boldsymbol{A}_i\boldsymbol{x}_a+\boldsymbol{B}_iV_d\right)dT_e+\boldsymbol{x}_{e|n}\right)+\boldsymbol{B}_iV_d\right)(1-d)\,T_e \\ &+\left(\boldsymbol{A}_i\boldsymbol{x}_a+\boldsymbol{B}_iV_d\right)dT_e+\boldsymbol{x}_{e|n} \\ \triangleq& H_{i,j}(\boldsymbol{x}_n, d)\end{aligned} \tag{2}$$

where $H_{i,j}$ is the discrete function, and d presents the duty cycle of ith operating state. $\boldsymbol{x}_{e|n}$ and $\boldsymbol{x}_{e|n+1}$ are the initial and final values of a whole discrete-time mapping cycle.

2) Approximate Discrete-Time Model: When the sampling instants are fixed at the interactions of the control signal and carrier, an approximate discrete-time model is proposed in [31]. Three basic dc–dc converters: buck, boost, and buck-boost converter are analyzed and there are only two operating states during a switching period.

For the leading-edge modulation, one can obtain

$$\begin{aligned}\boldsymbol{x}\left[(n+1)T_s+T_{sp}\right] &= e^{\boldsymbol{A}_2 T_{sp}} e^{\boldsymbol{A}_1 (T_s-T_{sp})} x\left(nT_s+T_{sp}\right) \\ &+ e^{\boldsymbol{A}_2 T_{sp}} \int_0^{T_s-T_{sp}} e^{\boldsymbol{A}_1 \tau} \boldsymbol{B}_1 v_{\text{in}} d\tau \\ &+ \int_0^{T_{sp}} e^{\boldsymbol{A}_2 \tau} \boldsymbol{B}_2 v_{\text{in}} d\tau \end{aligned} \tag{3}$$

where T_s represents the operating period. T_{sp} is the duration from the start of the period to the sampling instant. For the trailing-edge modulation, one can obtain

$$\begin{aligned}\boldsymbol{x}\left[(n+1)T_s+T_{sp}\right] &= e^{\boldsymbol{A}_1 T_{sp}} e^{\boldsymbol{A}_2 (T_s-T_{sp})} x\left(nT_s+T_{sp}\right) \\ &+ e^{\boldsymbol{A}_1 T_{sp}} \int_0^{T_s-T_{sp}} e^{\boldsymbol{A}_2 \tau} \boldsymbol{B}_2 v_{\text{in}} d\tau \\ &+ \int_0^{T_{sp}} e^{\boldsymbol{A}_1 \tau} \boldsymbol{B}_1 v_{\text{in}} d\tau. \end{aligned} \tag{4}$$

The approximate expressions of $e^{\boldsymbol{A}iTsp}$ and $e^{\boldsymbol{A}i(Ts-Tsp)}$ are obtained by using the Taylor series (only the first-order term is considered).

3) Two-Time Scale Modeling: To mitigate the zero average state variable problem, a full-order discrete-time model using two-time scale is developed for the hybrid system that consists of slow and fast variables in [32]. The inductor current on the primary side and the output voltage of the system are considered as the fast state variable and slow state variable, respectively. Based on the two-time scale theory, the steady-state solution of the system is obtained.

B. Limitations in High-Order WPT Systems

The limitations of the model in [30] are the difficulty in achieving discretization in both CCM and DCM, and the lack of uniform criteria for T_e selection. When the Euler method is adopted in high-order systems such as the *LCC-LCC* WPT system, strong coupling of variables will lead to the failure of the modeling.

The approximate discrete-time modeling proposed in [31] is only applicable to low-order systems. Besides, the sampling time is fixed at a point in the switching period, which leads to poor scalability of the application scenario.

The full-order discrete-time model in [32] can mitigate the low accuracy of the small-signal average modeling at high frequency. However, the model consists of two reference variables, it is not applicable to dc–dc converters that operate at a low frequency. Besides, the two-time scale model is limited to phase-shift control.

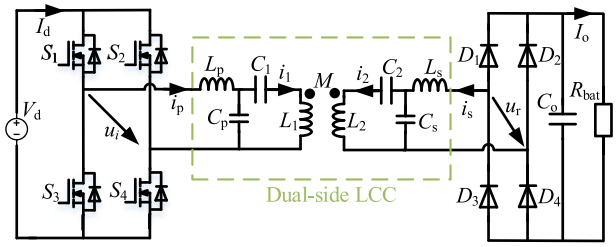

Fig. 2. Dual-side *LCC* compensated WPT system [1].

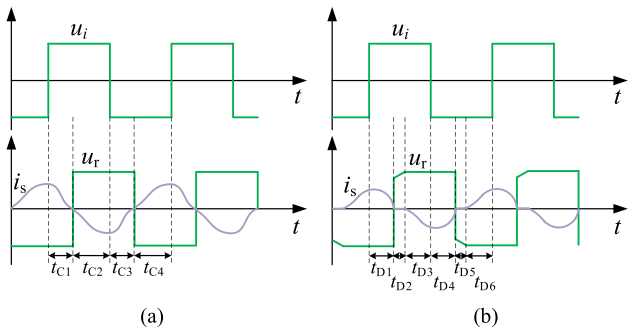

Fig. 3. Waveforms of the dual-side *LCC* compensated WPT system. (a) CCM. (b) DCM.

III. Proposed IFSM Model

In this section, the core idea of the IFSM model is explained. Due to its high-order characteristics, the *LCC-LCC* compensated WPT system is taken as an example to present the derivation process of the proposed model. The accuracy of the proposed model is verified and compared in time-domain simulations.

A. Analysis of the Dual-Side LCC Compensated WPT System

Fig. 2 shows the circuit of a dual-side *LCC* WPT system. L_1 and L_2 are the coil inductances of the transmitting and receiving coils, respectively. L_p, C_p, C_1 and L_s, C_s, C_2 are the compensation inductors and capacitors, respectively. R_{bat} is the equivalent resistance of the battery packs. V_d is the dc input voltage. The full-bridge inverter consists of four power MOSFETs S_1–S_4, and the rectifier consists of four diodes D_1–D_4. The quality factors of capacitors and inductors are high enough thus their parasitic resistances are neglected.

B. Core Idea of the Discrete-Time Modeling

Fig. 3 shows the waveforms of the output voltage of the inverter u_i, the input voltage of the rectifier u_r, and the output current of the compensation network i_s in CCM and DCM. There are four operating states in CCM and six operating states in DCM. t_{C1}–t_{C4} and t_{D1}–t_{D6} are the duration time of each operating state. It is obvious that $T_s = t_{C1}+t_{C2}+t_{C3}+t_{C4} = t_{D1}+t_{D2}+t_{D3}+t_{D4}+t_{D5}+t_{D6}$.

Fig. 4 takes two operating periods T_s as an example to illustrate the differences between the traditional SM model and IFSM model. In Fig. 4, the inner green circles and the outer purple circles represent the mapping sequences of the IFSM and

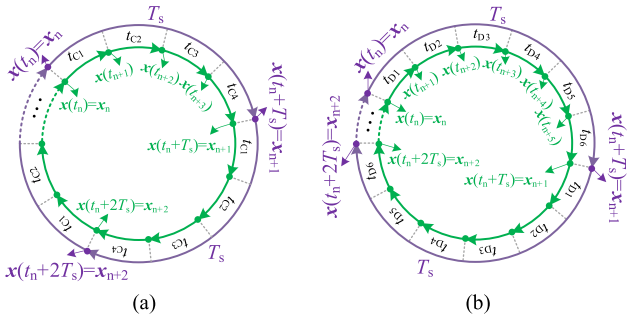

Fig. 4. Comparison of mapping points of traditional SM and IFSM. (a) CCM. (b) DCM.

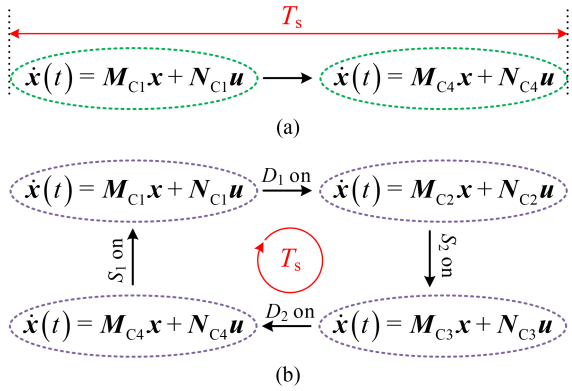

Fig. 5. Difference of the operating states contained in the SM and IFSM model. (a) SM. (b) IFSM.

SM models, respectively. Time t increases with the direction of the arrows. Each green and purple dot represents a discrete-time mapping point. In the steady state, the discrete-time mapping points of SM and IFSM repeat periodically.

One of the improvements of the IFSM can be concluded in the selection of discrete-time mapping points.

In CCM, which is shown in Fig. 4(a), the mapping time instants of the SM are t_n, t_n+T_s, t_n+2T_s, …, and the discrete-time mapping results of the SM model can be expressed as $\boldsymbol{x}_n = \boldsymbol{x}(t_n)$, $\boldsymbol{x}_{n+1} = \boldsymbol{x}(t_n+T_s)$, $\boldsymbol{x}_{n+2} = \boldsymbol{x}(t_n+2T_s)$, …. The discretization of the SM model is achieved according to the operating period T_s, which means that the step size remains constant as the period T_s. Different from the periodic mapping, the IFSM model maps according to the operating states of the WPT system. It can be seen from Figs. 3(a) and 4(a) that there are four states of the system in CCM, and the durations are t_{C1}–t_{C4}. The mapping time instants of the IFSM are t_n, t_n+t_{C1}, $t_n+t_{C1}+t_{C2}$, $t_n+t_{C1}+t_{C2}+t_{C3}$, t_n+T_s, $t_n+T_s+t_{C1}$, $t_n+T_s+t_{C1}+t_{C2}$, $t_n+T_s+t_{C1}+t_{C2}+t_{C3}$, t_n+2T_s, …. The mapping results of the IFSM model can be expressed as $\boldsymbol{x}_n = \boldsymbol{x}(t_n)$, $\boldsymbol{x}(t_n+t_{C1})$, $\boldsymbol{x}(t_n+t_{C1}+t_{C2})$, $\boldsymbol{x}(t_n+t_{C1}+t_{C2}+t_{C3})$, $\boldsymbol{x}_{n+1} = \boldsymbol{x}(t_n+T_s)$, $\boldsymbol{x}(t_n+T_s+t_{C1})$, $\boldsymbol{x}(t_n+T_s+t_{C1}+t_{C2})$, $\boldsymbol{x}(t_n+T_s+t_{C1}+t_{C2}+t_{C3})$, $\boldsymbol{x}_{n+2} = \boldsymbol{x}(t_n+2T_s)$, …. What is more, the discretization step sizes of the IFSM model are variable based on the operating states of the system. The problems mentioned in Section II such as the selection of discretization step size are avoided.

Another improvement is that when the operating state changes, the IFSM model contains more information of the system than the traditional periodic mapping, ensuring higher accuracy.

Fig. 5 presents the operating state transition information of the *LCC-LCC* WPT system contained in the SM model and IFSM model in CCM. To distinguish from the symbolic representations in Section II, the matrices describing the *LCC-LCC* system are denoted as $\boldsymbol{M}$ and $\boldsymbol{N}$. The mapping points of the IFSM model are the time instants when the operating state changes. Thus, the information of each operating state needs to be considered in the model to ensure accuracy. Specifically, during one operating period T_s, the information of four operating states is indicated by using the matrices $\boldsymbol{M}_{C1}$, $\boldsymbol{M}_{C2}$, $\boldsymbol{M}_{C3}$, $\boldsymbol{M}_{C4}$ and $\boldsymbol{N}_{C1}$, $\boldsymbol{N}_{C2}$, $\boldsymbol{N}_{C3}$, and $\boldsymbol{N}_{C4}$ in the IFSM model. However, it can be seen in Figs. 4(a) and 5(a) that the traditional SM model only contains information of the first and last state during one operating period T_s, which are indicated by the system matrices $\boldsymbol{M}_{C1}$ and $\boldsymbol{M}_{C4}$, input matrices $\boldsymbol{N}_{C1}$ and $\boldsymbol{N}_{C4}$. The omission of state information leads to low accuracy of the traditional SM model.

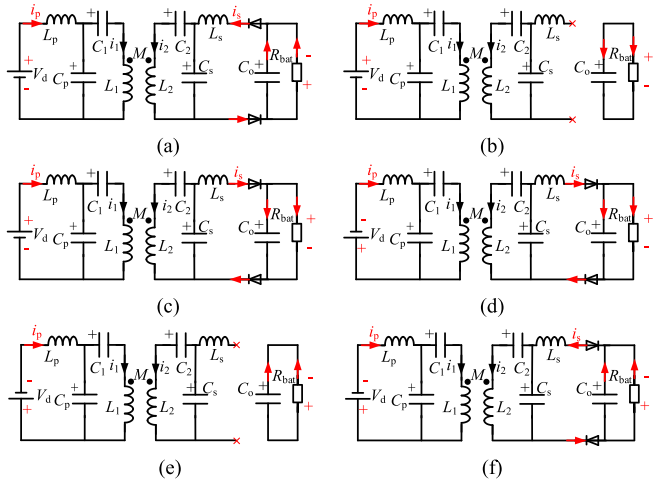

Fig. 6. Equivalent circuits for different intervals in DCM. (a) t_{D1}. (b) t_{D2}. (c) t_{D3}. (d) t_{D4}. (e) t_{D5}. (f) t_{D6}.

In conclusion, the traditional SM model only focuses on the behaviors in periodic time instants nT_s, which will lose the details of multiple state changes during one operating period. The IFSM model reveals all the operating states of the system in the whole operating frequency and load range. As shown in Fig. 5, the improved discrete-time model has at least two and four more sampling points than the traditional mapping in CCM and DCM, respectively. Moreover, different from the discrete-time sequences with fixed step size, the IFSM model samples according to state changes of the system, and then maps uniquely to points in the time domain.

C. Derivation of the Proposed Model

For the dual-side *LCC* compensated WPT system, the current i_s will be discontinuous when the load resistance R_{bat} is large to a specific value. Fig. 6 shows the equivalent circuits of different operating states in DCM. In this part, the proposed IFSM model that focuses on all the different operating states is established according to the waveforms of the system shown in Fig. 3.

TABLE I
FOUR OPERATING STATES IN CCM

Subinterval	t_{C1}	t_{C2}	t_{C3}	t_{C4}
u_i	P	P	N	N
i_p	P	P	N	N
u_r	N	P	P	N
i_s	P	N	N	P

P: positive; N: negative.

TABLE II
SIX OPERATING STATES IN DCM

Subinterval	t_{D1}	t_{D2}	t_{D3}	t_{D4}	t_{D5}	t_{D6}
u_i	P	P	P	N	N	N
i_p	P	P	P	N	N	N
u_r	N	P	P	P	N	N
i_s	P	Z	N	N	Z	P

P: positive; N: negative; Z: zero.

When the system operates in the CCM shown in Fig. 3(a) and the reference directions of the voltages and currents are defined in Fig. 2, there are four states during one operating period, which are presented in Table I. And the switching behaviors (on and off times) of the diode in CCM can be obtained according to the phase relationship analyzed in [1].

To present the derivation of the proposed model, the operating state in the subinterval t_{C1} is analyzed in detail. The differential equations of the system can be obtained as

$$\frac{di_p}{dt} = -\frac{1}{L_p}u_{C_p} + \frac{1}{L_p}V_d,\ \frac{du_{C_p}}{dt} = \frac{1}{C_p}i_p - \frac{1}{C_p}i_1 \quad (5)$$

$$\frac{du_{C_1}}{dt} = \frac{1}{C_1}i_1,\ \frac{du_{C_2}}{dt} = \frac{1}{C_2}i_2 \quad (6)$$

$$\frac{du_{C_s}}{dt} = -\frac{1}{C_s}i_2 - \frac{1}{C_s}i_s,\ \frac{di_s}{dt} = -\frac{1}{L_s}u_{C_s} + \frac{1}{L_s}u_{C_o} \quad (7)$$

$$\frac{di_1}{dt} = \frac{L_2}{\Delta}\left(u_{C_p} - u_{C_1}\right) - \frac{M}{\Delta}\left(u_{C_s} - u_{C_2}\right) \quad (8)$$

$$\frac{di_2}{dt} = \frac{L_1}{\Delta}\left(u_{C_s} - u_{C_2}\right) - \frac{M}{\Delta}\left(u_{C_p} - u_{C_1}\right) \quad (9)$$

$$\frac{du_{C_0}}{dt} = -\frac{1}{C_o}i_s + \frac{1}{R_{bat}C_o}u_{C_o} \quad (10)$$

where $\Delta = L_1L_2 - M^2$.

Choose $\boldsymbol{x} = [i_p\ u_{Cp}\ u_{C1}\ i_1\ i_2\ u_{C2}\ u_{Cs}\ i_s\ u_{Co}]^T$ as the state variable of the system, and the input vector can be set as $\boldsymbol{u}(t) = u_i(t)$. According to (5)–(10), the state-space model will be described as

$$\dot{\boldsymbol{x}}(t) = \boldsymbol{M}_{C_i}\cdot\boldsymbol{x}(t) + \boldsymbol{N}_{C_i}\cdot\boldsymbol{u}(t) \quad (11)$$

where i represents the ith operating states in CCM.

The solution of (11) is

$$\boldsymbol{x}(t) = \boldsymbol{\Phi}_{C_i}(t)\boldsymbol{x}_0 + \boldsymbol{M}_{C_i}^{-1}\left(\boldsymbol{\Phi}_{C_i}(t) - \boldsymbol{E}\right)\boldsymbol{N}_{C_i}V_d \quad (12)$$

where $\boldsymbol{x}_0 = \boldsymbol{x}(t)|_{t=t0}$, t_0 can be set to any time instant, and $\boldsymbol{\Phi}_{C_i}(t) = e^{\boldsymbol{M}_{C_i}t_{C_i}}$ $(i = 1, 2, 3, 4)$, $\boldsymbol{E}$ is the identity matrix, $\boldsymbol{M}_{C1}$ and $\boldsymbol{N}_{C1}$ are given in the Appendix.

The waveforms of u_i, u_r, and i_s are symmetrical, i.e., state intervals $t_{C1} = t_{C3}$, $t_{C2} = t_{C4}$, system matrices $\boldsymbol{M}_{C1} = \boldsymbol{M}_{C2} = \boldsymbol{M}_{C3} = \boldsymbol{M}_{C4}$, and control matrices $\boldsymbol{N}_{C1} = \boldsymbol{N}_{C2} = -\boldsymbol{N}_{C3} = -\boldsymbol{N}_{C4}$. The matrix $\boldsymbol{M}_{Ci}$ is only determined by the switching states of the rectifier and $\boldsymbol{N}_{Ci}$ are both relevant to the states of the inverter and rectifier.

The initial sampling time is $t_0 = nT_s$ and $T_s = t_{C1}+t_{C3}+t_{C2}+t_{C4}$, one can obtain the analytical solution of the IFSM model during one operating period T_s

$$\boldsymbol{x}(nT_s + t_{C1}) = \boldsymbol{\Phi}_{C1}(t)\boldsymbol{x}|_0 = nT_s + \boldsymbol{M}_{C1}^{-1}\left(\boldsymbol{\Phi}_{C1}(t) - \boldsymbol{E}\right)\boldsymbol{N}_{C1}V_d \quad (13)$$

$$\boldsymbol{x}(nT_s + t_{C1} + t_{C2}) = \boldsymbol{\Phi}_{C2}(t)\boldsymbol{x}|_{t=nT_s+t_{C1}} + \boldsymbol{M}_{C2}^{-1}\left(\boldsymbol{\Phi}_{C2}(t) - \boldsymbol{E}\right)\boldsymbol{N}_{C2}V_d \quad (14)$$

$$\boldsymbol{x}\left(\left(n+\frac{1}{2}\right)T_s + t_{C3}\right) = \boldsymbol{\Phi}_{C3}(t)\boldsymbol{x}|_{t=\left(n+\frac{1}{2}\right)\tau_s} + \boldsymbol{M}_{C3}^{-1}\left(\boldsymbol{\Phi}_{C3}(t) - \boldsymbol{E}\right)\boldsymbol{N}_{C3}V_d \quad (15)$$

$$\boldsymbol{x}((n+1)T_s) = \boldsymbol{x}\left(\left(n+\frac{1}{2}\right)T_s + t_{C3} + t_{C4}\right) = \boldsymbol{\Phi}_{C4}(t)\boldsymbol{x}|_{t=\left(n+\frac{1}{2}\right)T_s+t_{C3}} + \boldsymbol{M}_{C4}^{-1}\left(\boldsymbol{\Phi}_{C4}(t) - \boldsymbol{E}\right)\boldsymbol{N}_{C4}V_d. \quad (16)$$

In (12)–(16), the matrix $\boldsymbol{\Phi}_{C_i}(t) = e^{\boldsymbol{M}_{C_i}t_{C_i}}$ can be rewritten by $\hat{\boldsymbol{\Phi}}_{C_i}(t) = \boldsymbol{E} + t_{C_i}\boldsymbol{M}_{C_i}\boldsymbol{\Psi}_n$, where Ψ_n is expressed as

$$\boldsymbol{\Psi}_n = \boldsymbol{E} + \frac{1}{2!}\boldsymbol{M}_{C_i}t_{C_i} + \frac{1}{3!}(\boldsymbol{M}_{C_i}t_{C_i})^2 + \cdots + \frac{1}{n!}(\boldsymbol{M}_{C_i}t_{C_i})^{n-1} \quad (17)$$

and $\Psi_\infty = \boldsymbol{M}_{Ci}^{-1}(\Phi_{Ci} - \boldsymbol{E})$. By selecting a proper n, (17) can provide arbitrary accuracy in numerical calculation.

Similarly, when the coupling coefficient k decreases dramatically or the equivalent resistance R_{bat} of the battery packs becomes large to a specific value, the compensation network will operate in DCM, which is shown in Fig. 3(b). And there will be six intervals t_{D1}–t_{D6}, which are presented in Table II.

The solution of one discrete-time mapping period T_s can be obtained as

$$\boldsymbol{x}_{n+1} = \boldsymbol{J}\boldsymbol{x}_n + \boldsymbol{K}\boldsymbol{u}(t) \quad (18)$$

where

$$\boldsymbol{J} = e^{\boldsymbol{M}_{D6}t_{D6}}e^{\boldsymbol{M}_{D5}t_{D5}}e^{\boldsymbol{M}_{D4}t_{D4}}e^{\boldsymbol{M}_{D3}t_{D3}}e^{\boldsymbol{M}_{D2}t_{D2}}e^{\boldsymbol{M}_{D1}t_{D1}},$$

$$\boldsymbol{K} = e^{\boldsymbol{M}_{D6}t_{D6}}e^{\boldsymbol{M}_{D5}t_{D5}}e^{\boldsymbol{M}_{D4}t_{D4}}e^{\boldsymbol{M}_{D3}t_{D3}}e^{\boldsymbol{M}_{D2}t_{D2}}\boldsymbol{M}_{D1}^{-1} \times \left(e^{\boldsymbol{M}_{D1}t_{D1}} - \boldsymbol{E}\right)\boldsymbol{N}_{D1} + e^{\boldsymbol{M}_{D6}t_{D6}}e^{\boldsymbol{M}_{D5}t_{D5}}e^{\boldsymbol{M}_{D4}t_{D4}}e^{\boldsymbol{M}_{D3}t_{D3}} \times \int_0^{t_{D2}} e^{\boldsymbol{M}_{D2}(t_{D2}-\tau)}\boldsymbol{N}_{D2}d\tau + e^{\boldsymbol{M}_{D6}t_{D6}}e^{\boldsymbol{M}_{D5}t_{D5}}e^{\boldsymbol{M}_{D4}t_{D4}}\boldsymbol{M}_{D3}^{-1}\left(e^{\boldsymbol{M}_{D3}t_{D3}} - \boldsymbol{E}\right)\boldsymbol{N}_{D3} + e^{\boldsymbol{M}_{D6}t_{D6}}e^{\boldsymbol{M}_{D5}t_{D5}}\boldsymbol{M}_{D4}^{-1}\left(e^{\boldsymbol{M}_{D4}t_{D4}} - \boldsymbol{E}\right)\boldsymbol{N}_{D4}$$

$$+ e^{\boldsymbol{M}_{\mathrm{D6}} t_{\mathrm{D6}}} \int_0^{t_{\mathrm{D5}}} e^{\boldsymbol{M}_{\mathrm{D5}}(t_{\mathrm{D5}}-\tau)} \boldsymbol{N}_{\mathrm{D5}} d\tau$$
$$+ \boldsymbol{M}_{\mathrm{D6}}^{-1} \left(e^{\boldsymbol{M}_{\mathrm{D6}} t_{\mathrm{D6}}} - \boldsymbol{E}\right) \boldsymbol{N}_{\mathrm{D6}}.$$

Matrices $\boldsymbol{M}_{\mathrm{D}i}$ and $\boldsymbol{N}_{\mathrm{D}i}$ ($i = 1, 2, 3, 4, 5, 6$) are also given in the Appendix, and $\boldsymbol{M}_{\mathrm{D1}} = \boldsymbol{M}_{\mathrm{D3}} = \boldsymbol{M}_{\mathrm{D4}} = \boldsymbol{M}_{\mathrm{D6}}$, $\boldsymbol{M}_{\mathrm{D2}} = \boldsymbol{M}_{\mathrm{D5}}$, $\boldsymbol{N}_{\mathrm{D1}} = \boldsymbol{N}_{\mathrm{D2}} = \boldsymbol{N}_{\mathrm{D3}} = -\boldsymbol{N}_{\mathrm{D4}} = -\boldsymbol{N}_{\mathrm{D5}} = -\boldsymbol{N}_{\mathrm{D6}}$.

In CCM, when given the system parameters, the analytical solution of the IFSM can be easily obtained by the expressions (13)–(17). But when the system operates in DCM, there are integral elements existing in (18), which leads to irreversibility and nonintegrability of the high-order matrix $\boldsymbol{K}$ and makes it impossible to obtain the analytical solution directly. To make the discrete-time IFSM model applicable to online calculation, simplification for $\boldsymbol{K}$ with high accuracy is also expected.

The integral element $\boldsymbol{F} = \int_0^{t_{\mathrm{D}i}} e^{\boldsymbol{M}_{\mathrm{D}i}\tau} d\tau (i = 2 \text{ and } 5)$ can be further expressed as

$$\hat{\boldsymbol{F}} = t_{D_i} \boldsymbol{\Psi}_n. \tag{19}$$

And with the help of (17), the solution of IFSM in the steady state can be calculated by

$$\boldsymbol{x}_{\mathrm{ss}} = \left(\boldsymbol{E} - \hat{\boldsymbol{J}}\right)^{-1} \hat{\boldsymbol{K}} V_{\mathrm{d}} \tag{20}$$

where $\boldsymbol{J}$ and $\boldsymbol{K}$ are rewritten as $\hat{\boldsymbol{J}}$ and $\hat{\boldsymbol{K}}$ by using (17).

When the system runs into states (c)–(f), the polarities of the voltage V_{d} and current i_2 are changed. Notably, because the variables related to operating frequency and the operating states are all considered in the IFSM model, the process described in this part can be used for the full-power range and full-frequency range of the system.

In DCM, the durations t_{D1} and t_{D4} can be calculated according to the phase relationship of the dual-side *LCC* compensation network, which means the off time of the diode is obtained. Before the determination of the on time, one can know that $t_{\mathrm{D2}} = t_{\mathrm{D5}}$, $t_{\mathrm{D3}} = t_{\mathrm{D6}}$, $t_{\mathrm{D1}}+t_{\mathrm{D2}}+t_{\mathrm{D3}} = t_{\mathrm{D4}}+t_{\mathrm{D5}}+t_{\mathrm{D6}} = T_{\mathrm{s}}/2$, once t_{D2} is obtained, t_{D3} will be expressed as $T_{\mathrm{s}}/2$-t_{D2}-t_{D1}. Finally, the only duration time of the subinterval needs to be solved is t_{D2}. Based on (18)–(20), the solutions of the first two subintervals t_{D1} and t_x (t_{D2} needs to be solved, thus it is redefined as t_x) can be expressed as

$$\boldsymbol{x}_{\mathrm{ss1}} = \boldsymbol{x}_{\mathrm{ss}}(nT_{\mathrm{s}}+t_{\mathrm{D1}}) = \boldsymbol{\Phi}_{\mathrm{D1}}(t)\,\boldsymbol{x}|_{t_0=nT_{\mathrm{s}}} + \boldsymbol{M}_{\mathrm{D1}}^{-1}\left(\boldsymbol{\Phi}_{\mathrm{D1}}(t) - \boldsymbol{E}\right)\boldsymbol{N}_{\mathrm{D1}} V_{\mathrm{d}} \tag{21}$$

$$\boldsymbol{x}_{\mathrm{ss2}} = \boldsymbol{x}_{\mathrm{ss}}(nT_{\mathrm{s}} + t_{\mathrm{D1}} + t_x) = \boldsymbol{\Phi}_{\mathrm{D2}}(t)\,\boldsymbol{x}|_{\mathrm{t}=nT_{\mathrm{s}}+t_{\mathrm{D1}}} + \int_0^{t_x} e^{\boldsymbol{M}_{\mathrm{D2}}(t_x-\tau)} \boldsymbol{N}_{\mathrm{D2}} V_{\mathrm{d}} d\tau \tag{22}$$

where t_x is an unknown variable.

According to the characteristic of the system in DCM, two conditions of the switching behavior that occurs at the on time of the diode are $i_{\mathrm{s}|t\,=\,nTs+\,tD2+tD1} = 0$ and $u_{\mathrm{r}|t\,=\,nTs+\,tD2+tD1} \geq u_{Co}$ (the output voltage u_{r} of the compensation network is always lower than the load voltage u_{Co} in DCM because of the voltage distortion, once u_{r} is higher than u_{Co}, the diode will switch ON).

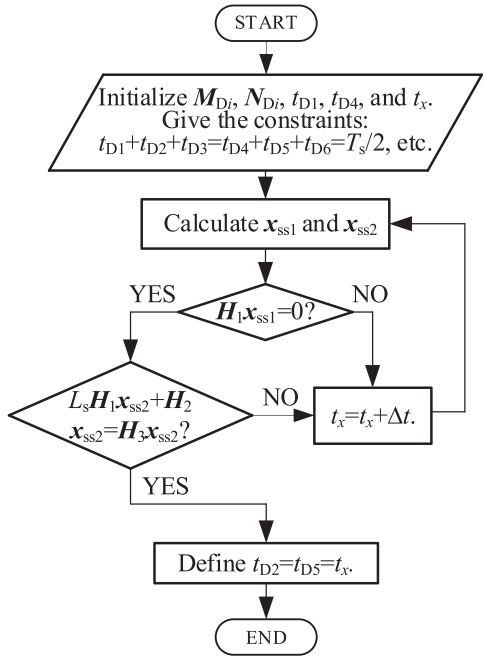

Fig. 7. Flowchart of on-time calculation of the diode in DCM.

Thus, the value of $t_x = t_{\mathrm{D2}}$ can be uniquely determined only when both conditions are met simultaneously. The boundary conditions of the on-time calculation can be further expressed as

$$\boldsymbol{H}_1\boldsymbol{x}_{ss1} = 0 \tag{23}$$

$$L_{\mathrm{s}}\boldsymbol{H}_1\boldsymbol{x}_{ss2} + \boldsymbol{H}_2\boldsymbol{x}_{ss2} \geq \boldsymbol{H}_3\boldsymbol{x}_{ss2} \tag{24}$$

where $\boldsymbol{H}_1 = [00\ 00\ 00\ 01\ 0]^T$, $\boldsymbol{H}_2 = [00\ 00\ 00\ 10\ 0]^T$, and $\boldsymbol{H}_3 = [00\ 00\ 00\ 00\ 1]^T$.

The flowchart of the on-time calculation of the diode in DCM is shown in Fig. 7. The time instant corresponding to the rising edge of the inverter voltage is marked as t_0. And the iteration step size of Δt is defined as 20 ns (1/10 of the dead time t_{d} in the experiments). To ensure the validity of the results obtained in Fig. 7, it is necessary to compare t_x with $T_{\mathrm{s}}/4$. If t_x is greater than $T_{\mathrm{s}}/4$, then it is essential to redefine t_0 as $t_0+T_{\mathrm{s}}/4$, which is because the uniqueness of the operating state of the first subinterval has changed.

D. Schematic Diagram of the IFSM Model Calculation

The IFSM model in DCM is taken as an example to explain the calculation process, $\boldsymbol{x}_n$ and $\boldsymbol{x}_{n+1}$ are the initial and final values of one discrete-time mapping cycle, respectively. $\boldsymbol{x}(t_{\mathrm{n}}+d_iT_{\mathrm{s}})$ ($i = 1, 2, \ldots, 6$, $d_iT_{\mathrm{s}} = t_{\mathrm{D}i}$) represents the value of ith stage, where d_i is the duty ratio of the ith stage shown in Fig. 8. The final value of the first stage $\boldsymbol{x}(t_{\mathrm{n}}+d_1T_{\mathrm{s}})$ can be derived from the initial value $\boldsymbol{x}(t_{\mathrm{n}})$, and the value of $\boldsymbol{x}(t_{\mathrm{n}}+d_1T_{\mathrm{s}}+d_2T_{\mathrm{s}})$ can be derived from $\boldsymbol{x}(t_{\mathrm{n}}+d_1T_{\mathrm{s}})$. As expressed in (18), the final value of each other subinterval can be derived from $\boldsymbol{x}_n$.

Furthermore, different from the traditional approach of fitting waveforms by using many discrete-time mapping points, for the IFSM model within each discrete subinterval (i.e., each state

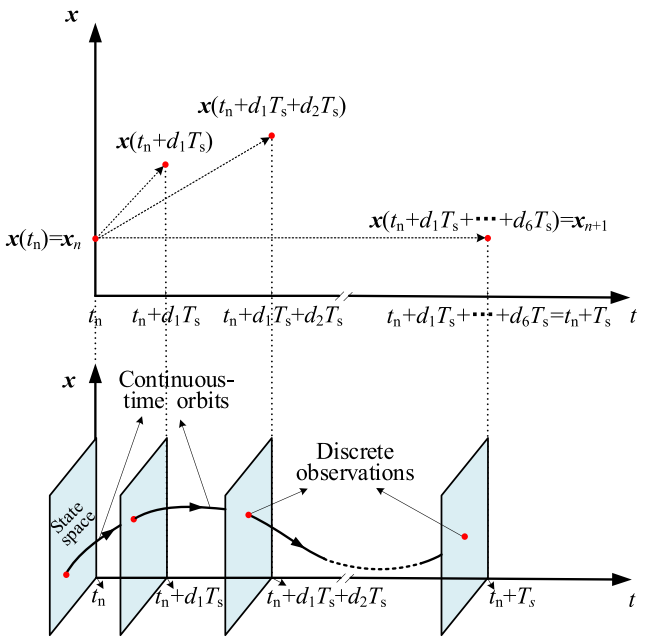

Fig. 8. Calculation process of the IFSM model in DCM.

change process), the system response is solved by using state transition matrices $\hat{\boldsymbol{J}}$ and $\hat{\boldsymbol{K}}$, and the response for one mapping period T_s is achieved through matrix iteration. In other words, using the state transition matrix $e^{\boldsymbol{M}_{\mathrm{D}i}t_{\mathrm{D}i}}$ to solve within a discrete subinterval yields a piecewise smooth continuous waveform. For example, the expressions of the first two continuous-time orbits shown in Fig. 8 can be expressed as

$$\boldsymbol{\Phi}_{\mathrm{D1}}(t)\,\boldsymbol{x}|_{t_n}+\boldsymbol{M}_{\mathrm{D1}}^{-1}\left(\boldsymbol{\Phi}_{\mathrm{D1}}(t)-\boldsymbol{E}\right)\boldsymbol{N}_{\mathrm{D1}}V_\mathrm{d},\quad t_n\le \mathrm{t}\le t_n+d_1T_\mathrm{s} \tag{25}$$

$$\boldsymbol{\Phi}_{\mathrm{D2}}(t)\,\boldsymbol{x}|_{t_n+d_1T_\mathrm{s}}+\boldsymbol{M}_{\mathrm{D2}}^{-1}\left(\boldsymbol{\Phi}_{\mathrm{D2}}(t)-\boldsymbol{E}\right)\boldsymbol{N}_{\mathrm{D2}}V_\mathrm{d},\quad t_n+d_1T_\mathrm{s}\le \mathrm{t}\le t_n+d_1T_\mathrm{s}+d_2T_\mathrm{s}. \tag{26}$$

In addition, for the selection of the initial mapping point within one mapping period, it can be either the start or end time of any operating state. For the convenience of analysis, the rising edge of the inverter voltage is chosen as the starting point for the full-power discrete-time mapping in this article.

E. Verification in Simulation

To present the superiority of the proposed IFSM model, a comparative study of the dual-side *LCC* WPT system defined by parameters listed in Table III is conducted by time-domain simulations. Fig. 9 shows the waveforms of output voltage, current of the inverter (u_i, i_p), and the input current of the rectifier (u_r, i_s) in CCM and DCM.

To show how well the IFSM model can describe the response of the system, the fitness ratio Q_fitness between results of different models A, and the true system output $\hat{A}$ is taken as the performance index to quantize the model accuracy. In this article, a total number of 10^4 model and time-domain

TABLE III
PARAMETERS OF THE *LCC-LCC* WPT SYSTEM

Symbol	Parameter	Value	Unit
L_p	Primary compensation inductor	23.5	μH
C_p	Primary parallel capacitor	149.2	nF
C_1	Primary series capacitor	32.8	nF
L_s	Secondary compensation inductor	23.2	μH
C_s	Secondary parallel capacitor	150.1	nF
C_2	Secondary series capacitor	50.7	nF
L_1	Self-inductance of transmitting coil	130.3	μH
L_2	Self-inductance of receiving coil	92.2	μH

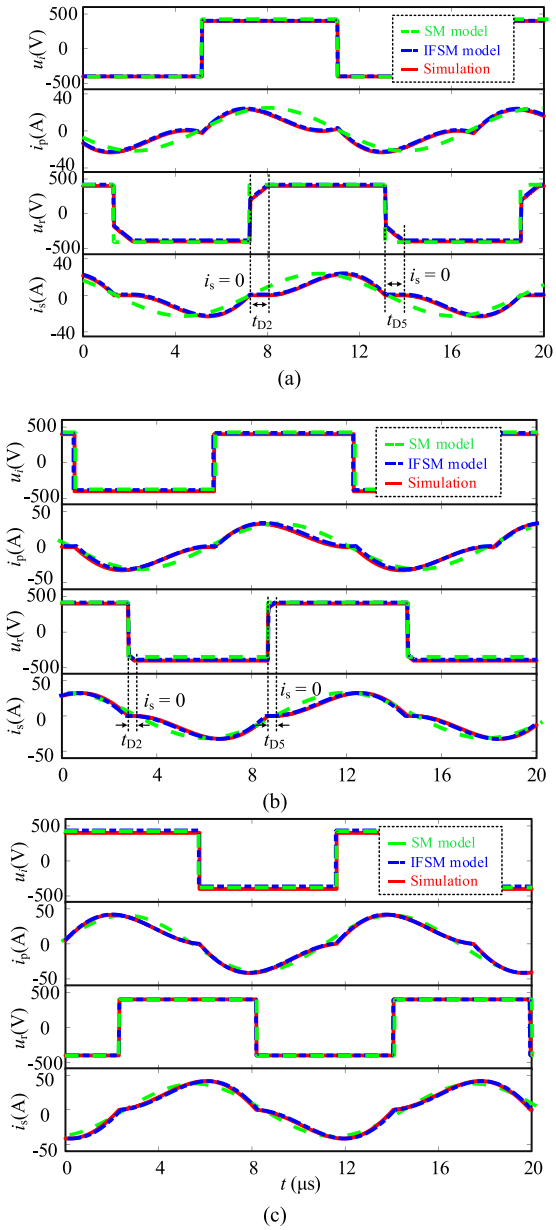

Fig. 9. Comparison of the waveforms obtained by the SM model, IFSM model, and simulations when $V_\mathrm{d}=400$ V and $f_\mathrm{s}=f_\mathrm{A}$. (a) $k=0.1$, DCM. (b) $k=0.15$, DCM. (c) $k=0.2$, CCM.

TABLE IV
FITNESS RATIOS OF DIFFERENT MODELS

Response	Fitness Ratio (%)					
	$k = 0.1$		$k = 0.15$		$k = 0.2$	
	SM	IFSM	SM	IFSM	SM	IFSM
u_i	98.40	98.45	98.79	98.88	98.22	99.00
i_p	49.46	98.10	70.05	98.43	84.56	98.32
u_r	86.12	98.33	89.05	98.51	98.27	98.19
i_s	50.28	98.29	71.66	98.44	85.49	98.32

simulation observations is used to present the accuracy index

$$Q_{\text{fitness}} = \left(1 - \frac{\left|\left|A - \hat{A}\right|\right|_2}{\left|\left|\hat{A} - \text{mean}\{\hat{A}\}\right|\right|_2}\right) \times 100\%. \tag{27}$$

The fitness ratios of the traditional SM model, the IFSM model, and the time-domain simulations are presented in Table IV.

When $k = 0.2$, the load is in CCM, both the SM model and IFSM model feature the simulation results well. However, when $k = 0.15$, the load is in DCM, the IFSM model shows high accuracy and slight errors occur with the traditional SM model. When $k = 0.1$, the IFSM model also features the simulation results very well, while obvious errors occur with the SM model. The longer the time in DCM is, the larger the errors of the SM model are. As for the output voltage of the compensation network, the SM model cannot feature the change in DCM. These results show the improved model outputs provide a good fitness to the system output (Q_{fitness} >98%). The traditional mapping points are located in the periodic time instants and the several operating states are lost in the SM model. Thus, the errors will occur when the system operates in DCM.

IV. ZCS POINTS ANALYSIS BASED ON THE IFSM MODEL

According to the analysis in Sections II and III, there is no approximation in the IFSM model, which makes it possible to calculate the ZCS points accurately. In this section, different from the analysis in [27] and [28], the ZCS frequencies of the inverter are obtained based on the IFSM model and ZCS curves with respect to operating frequency and coupling coefficient are analyzed.

A. ZCS Frequency Calculation Based on IFSM Model

If the system operates in CCM, for a steady sampling period, the initial state $\boldsymbol{x}_{\text{n}}$ and final state $\boldsymbol{x}_{\text{n+1}}$ satisfy the following expression:

$$\begin{aligned}\boldsymbol{x}_{n+1} &= \Gamma\left(\boldsymbol{x}_n, \text{t}_{\text{C1}}, \text{t}_{\text{C2}}, \text{t}_{\text{C3}}, \text{t}_{\text{C4}}\right)\\ &= \boldsymbol{\Phi}\left(\text{t}_{\text{C4}}\right)\boldsymbol{\Phi}\left(\text{t}_{\text{C3}}\right)\boldsymbol{\Phi}\left(\text{t}_{\text{C2}}\right)\boldsymbol{\Phi}\left(\text{t}_{\text{C1}}\right)\boldsymbol{x}_n\\ &\quad + \boldsymbol{\Phi}\left(\text{t}_{\text{C4}}\right)\boldsymbol{\Phi}\left(\text{t}_{\text{C3}}\right)\boldsymbol{\Phi}\left(\text{t}_{\text{C2}}\right)\boldsymbol{M}_{\text{C1}}^{-1}\left(\boldsymbol{\Phi}\left(\text{t}_{\text{C1}}\right) - \boldsymbol{E}\right)\boldsymbol{N}_{\text{C1}}V_{\text{d}}\\ &\quad + \boldsymbol{\Phi}\left(\text{t}_{\text{C4}}\right)\boldsymbol{\Phi}\left(\text{t}_{\text{C3}}\right)\boldsymbol{M}_{\text{C2}}^{-1}\left(\boldsymbol{\Phi}\left(\text{t}_{\text{C2}}\right) - \boldsymbol{E}\right)\boldsymbol{N}_{\text{C2}}V_{\text{d}}\\ &\quad + \boldsymbol{\Phi}\left(\text{t}_{\text{C4}}\right)\boldsymbol{M}_{\text{C3}}^{-1}\left(\boldsymbol{\Phi}\left(\text{t}_{\text{C3}}\right) - \boldsymbol{E}\right)\boldsymbol{N}_{\text{C3}}V_{\text{d}}\\ &\quad + \boldsymbol{M}_{\text{C4}}^{-1}\left(\boldsymbol{\Phi}\left(\text{t}_{\text{C4}}\right) - \boldsymbol{E}\right)\boldsymbol{N}_{\text{C4}}V_{\text{d}}.\end{aligned} \tag{28}$$

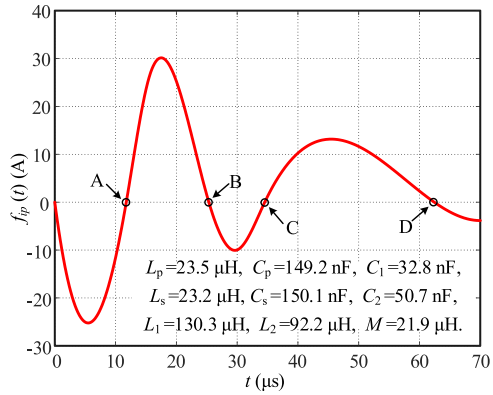

Fig. 10. Curve of fixed points of inverter current i_{p} when $k = 0.2$ and $V_{\text{d}} = V_{\text{bat}} = 400$ V.

TABLE V
INFORMATION OF THE FIRST FOUR ZCS POINTS

ZCS points	A	B	C	D
Time (μs)	11.77	25.34	34.54	62.42
Frequency (kHz)	84.95	39.46	28.95	16.02
THD (%)	6.43	80.87	165.22	268.40

By defining $\boldsymbol{M} = \boldsymbol{M}_{\text{C1}} = \boldsymbol{M}_{\text{C2}} = \boldsymbol{M}_{\text{C3}} = \boldsymbol{M}_{\text{C4}}$, $\boldsymbol{N} = \boldsymbol{N}_{\text{C1}} = \boldsymbol{N}_{\text{C2}} = \text{-}\boldsymbol{N}_{\text{C3}} = \text{-}\boldsymbol{N}_{\text{C4}}$, $\delta_1 = t_{\text{C1}} = t_{\text{C3}}$, $\delta_2 = t_{\text{C2}} = t_{\text{C4}}$, when $\boldsymbol{x}_{\text{n+1}} = \boldsymbol{x}_{\text{n}} = \boldsymbol{x}^*$ (the system operates in the steady state), one can obtain by solving (28)

$$\begin{aligned}\boldsymbol{x}^* &= \left(\boldsymbol{E} + \boldsymbol{\Phi}\left(\delta_2\right)\boldsymbol{\Phi}\left(\delta_1\right)\right)^{-1}\\ &\cdot\left[\boldsymbol{\Phi}\left(\delta_2\right)\boldsymbol{M}^{-1}\left(\boldsymbol{E} - \boldsymbol{\Phi}\left(\delta_1\right)\right)\boldsymbol{N}V_{\text{d}} + \boldsymbol{M}^{-1}\left(\boldsymbol{E} - \boldsymbol{\Phi}\left(\delta_2\right)\right)\boldsymbol{N}V_{\text{d}}\right].\end{aligned} \tag{29}$$

If only the inverter voltage and current are considered, there are two half symmetry periods, and the structure of the circuit does not change, (29) can be further simplified into the following:

$$\boldsymbol{x}^* = \left(\boldsymbol{E} + \boldsymbol{\Phi}\left(\frac{T_{\text{s}}}{2}\right)\right)^{-1}\left(\boldsymbol{E} - \boldsymbol{\Phi}\left(\frac{T_{\text{s}}}{2}\right)\right)\boldsymbol{M}^{-1}\boldsymbol{N}V_{\text{d}}. \tag{30}$$

Period T_{s} is taken as the independent variable in (30) instead of time t, which is one of the advantages of the IFSM model. To derive the ZCS points of the dual-side *LCC* compensated WPT system, the function of inverter current i_{p} can be obtained as

$$f_{i_{\text{p}}}(t) = \boldsymbol{G}\left(\boldsymbol{E} + \boldsymbol{\Phi}_1\left(\frac{t}{2}\right)\right)^{-1}\left(\boldsymbol{E} - \boldsymbol{\Phi}\left(\frac{t}{2}\right)\right)\boldsymbol{M}^{-1}\boldsymbol{N}V_{\text{d}} \tag{31}$$

where the response selection matrix $\boldsymbol{G} = [10\ 00\ 00\ 00\ 0]^T$.

By defining different selection matrices, one can obtain the expressions of different variables. It can be also observed from (31) that the solutions of different variables are independent of each other.

The curve of (31) is printed in Fig. 10 when the parameters used in this article are given. There are four ZCS points of current i_{p} (the zero solution is not considered), which are marked as A, B, C, and D. As illustrated in Table V, the corresponding periods of four points are 11.75, 25.34, 34.54, and 48.08 μs.

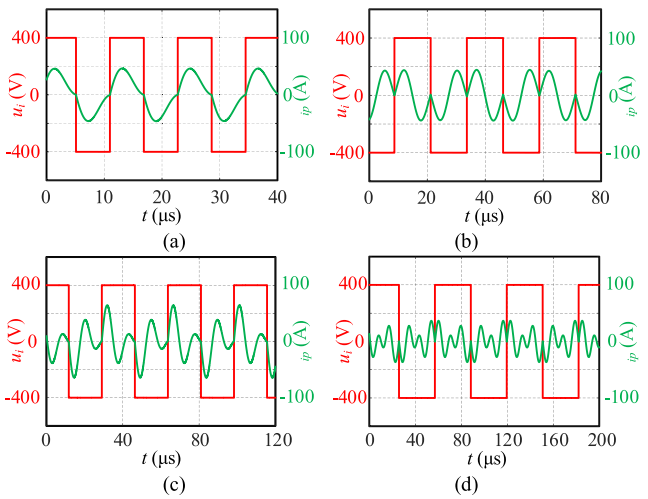

Fig. 11. Output voltage and current of the inverter operating at different ZCS frequencies. (a) 84.95 kHz. (b) 39.46 kHz. (c) 28.95 kHz. (d) 16.02 kHz.

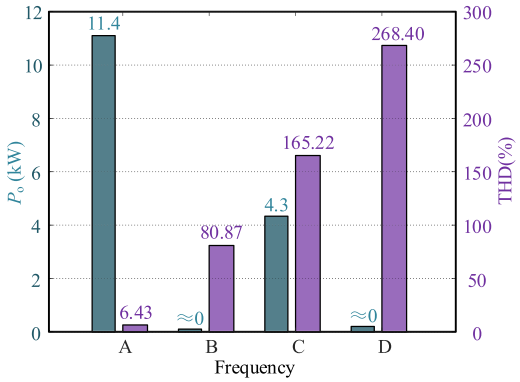

Fig. 12. Comparison of power transfer ability and THD of the inverter output current i_p when $k = 0.2$ and $V_d = V_{bat} = 400$ V.

Thus, their corresponding frequencies are 84.95, 39.46, 28.95, and 16.02 kHz, respectively.

B. Selection of the Optimal ZCS Point

Among the possible soft-switching points, it is important to determine the one that has the maximum power transfer capability. Fig. 11 shows the waveforms of output voltage and current at the four ZCS points obtained in simulations. Given the parameters listed in Fig. 10, the power transfer ability and THD when the system operates at the four points are illustrated in Fig. 12. When the system operates at frequencies B and D, if the load is 400-V battery packs, there is little power transferred to the load, which means they cannot be chosen as the operating frequencies of the inverter.

The frequency range is limited from 79 to 90 kHz in standard SAE J2954 of the EV WPT systems. Because of the lowest harmonic contents and a good match with the resonant frequency, point A is chosen as the reference operating frequency of the system to analyze the full-power and full-frequency characteristics.

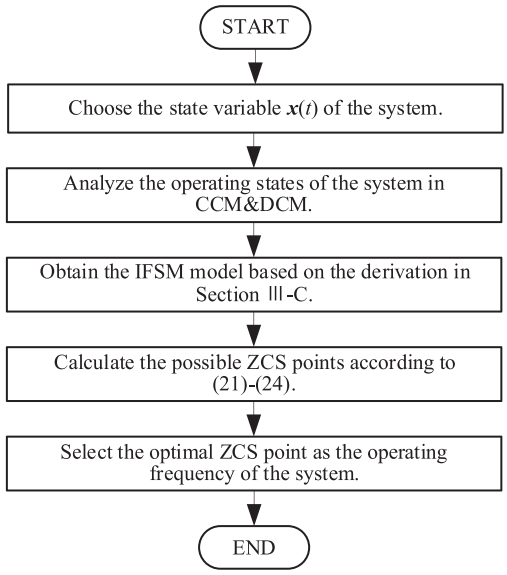

Fig. 13. Procedure of the optimal ZCS point selection.

It should be noted that the optimal ZCS point in this article is quite close to the resonant frequency, which is because one of the most important features of the WPT system is that it needs to operate at the resonant point to achieve zero phase angle (ZPA) and maximum efficiency [2]. In fact, there could be multiple frequencies that meet the required range when studying other compensation networks and nonisolated converters, and determining the optimal operating point requires further comparison.

Fig. 13 gives the selection procedure of the optimal ZCS points of the studied system. When studying the nonisolated converters such as buck-boost, cuk, and cascaded boost converters [19], the systems have relatively fewer variables, which leads to an increase in the applicability of the solutions. Besides, for the nonisolated converters, the resonant frequency is often not required. Thus, point B, C, or D could be also the optimal ones in different application scenarios.

C. ZCS Range Analysis

In practical applications, the positions of GA and VA are not always relatively fixed and the coupling coefficient k will also vary from 0.094 to 0.244 [25]. Moreover, during the charging process, control methods such as phase-shift control will lead to hard switching of the primary inverter without a cascaded dc–dc converter [29]. To minimize the circuit's reactive power and improve the dc–dc efficiency of the charging system, it is necessary to analyze the impact of the coupling coefficient on the ZCS points.

The ZCS current i_{p_ZCS} is the input current of the compensation network at nT_s, according to the IFSM model, one can obtain

$$i_{p\_ZCS} = i_p(nT_s) = i_p((n+1)T_s). \tag{32}$$

Fig. 14 shows the relationship between the frequency of point A and coupling coefficient k, where the results obtained from the traditional SM model, the IFSM model, and the time-domain

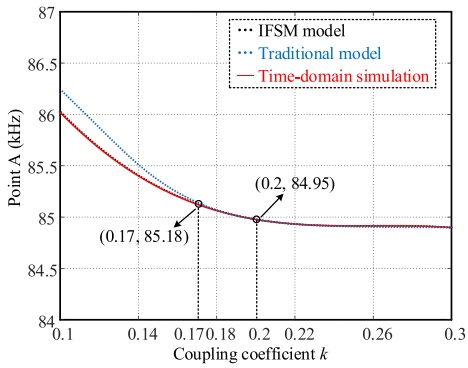

Fig. 14. Fitted curve of frequency A with respect to coupling coefficient k when $V_{\mathrm{bat}} = V_{\mathrm{d}} = 400$ V.

simulations are compared. The accuracy of the improved model is verified through the perfect match. The results of the traditional model deviate from the simulation result when $k < 0.17$, which is because several operating states are lost in DCM. If the operating frequency f_{s} traces the curve, especially when the charging current changes significantly in CV mode, the inverter will always achieve ZCS. In other words, the ZVS current is zero and the output voltage u_i and current i_{s} are in phase, ZPA is also achieved.

V. Boundaries of CCM/DCM

In this section, the IFSM model is used to analyze the discontinuous boundaries of the output current i_{s} by using the *LCC-LCC* WPT system as an example. It is helpful to clarify the applicability of the traditional SM model and IFSM model. Besides, to mitigate battery aging costs in dynamic energy management, it is necessary to derive the boundaries of the charging current for energy management of vehicle battery energy storage systems [26]. The IFSM model characterizes the system through matrices $\boldsymbol{M}_i$ and $\boldsymbol{N}_i$, which gives the possibility to derive accurate solutions.

A. Boundary Constraints

To ensure the accuracy of the boundary analysis, some constraints on the IFSM model and system characteristics need to be considered. The boundaries of CCM and DCM of the output current i_{s} with respect to the coupling coefficient k and battery resistance R_{bat} will be obtained under the constraint conditions.

1) Constraints on the IFSM Model: The equivalent series resistance of the passive components and active switches are not considered in the discrete-time model for simplification. The step size of the model calculation needs to be smaller than 1/10 of the dead time t_{d}.

2) Constraints on the System Characteristics: Phase constraint: In the dual-side *LCC* WPT system, the phase of the output voltage u_{r} lags the input voltage u_i, which is shown in Fig. 3(a), thus the range of phase α between u_{r} and u_i needs to be constrained within $(0, \pi/2)$. The phases among i_{p}, i_1, i_2, and i_{p} are also required to meet the constraints in [1].

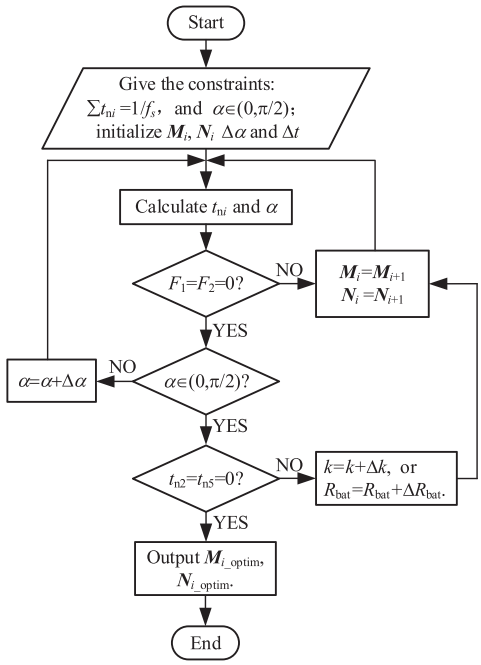

Fig. 15. Flowchart of CCM/DCM boundary calculation.

Time Interval Constraint: during the process of matrix solving, there are multiple results of $t_{\mathrm{n}i}$ $(i = 1, 2, \ldots)$ when the load condition and coupling coefficient are given. $t_{\mathrm{n}i}$ includes both $t_{\mathrm{D}i}$ and $t_{\mathrm{C}i}$. All the time intervals need to satisfy the constraint of the operating period T_{s}, which means $T_{\mathrm{s}} = t_{\mathrm{n}1}+t_{\mathrm{n}2}+\ldots$.

Boundary Condition Constraint: the inverter output current i_{p} needs to satisfy the following constraints to meet the ZCS operation:

$$F_1\left(\xi_1, \boldsymbol{x}_n\right) = \boldsymbol{G} f_{1,\xi_1}\left(\boldsymbol{x}_n\right) = 0 \tag{33}$$

$$F_2\left(\xi_2, \xi_1, \boldsymbol{x}_n\right) = \boldsymbol{G} f_{2,\xi_2}\left(\mathrm{f}_{1,\xi_1}\left(\boldsymbol{x}_n\right)\right) = 0 \tag{34}$$

where F_1 and F_2 are boundary functions, ξ_1 and ξ_2 represent the duration time of the inverter operating in the positive half period and the negative half period, respectively.

B. Steps for Boundary Calculation

The boundary analysis procedures can be summarized as the following four steps.

Step 1: Select the system variable and establish the IFSM model of the studied system in CCM and DCM (e.g., dual-side *LCC* compensated WPT system in this article), and obtain the solutions of different operating modes.

Step 2: Give the CCM/DCM boundary and model calculation constraints of the studied system, such as phase constraint, period constraint, frequency constraint, etc.

Step 3: Choose the target boundary parameters and set the ranges and iteration step sizes.

Step 4: Solve the matrices $\boldsymbol{M}_{i\_\mathrm{optim}}$ and $\boldsymbol{N}_{i\_\mathrm{optim}}$ according to the flowchart shown in Fig. 15.

Fig. 15 gives the flowchart of the calculation process. The iteration step sizes Δk and ΔR_{bat} are required much smaller

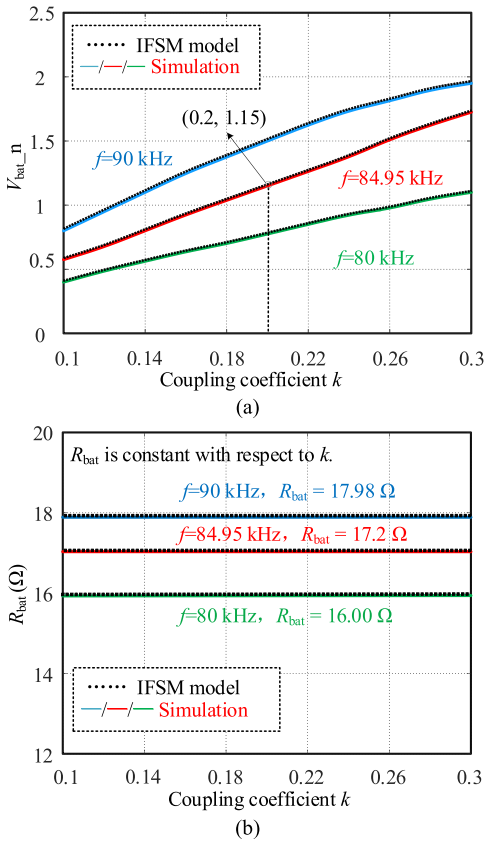

Fig. 16. Boundary voltage $V_{\mathrm{bat\_n}}$ and resistance R_{bat} with respect to coupling coefficient k at different frequencies when $V_{\mathrm{d}} = 400$ V. (a) $V_{\mathrm{bat\_n}}$. (b) R_{bat}.

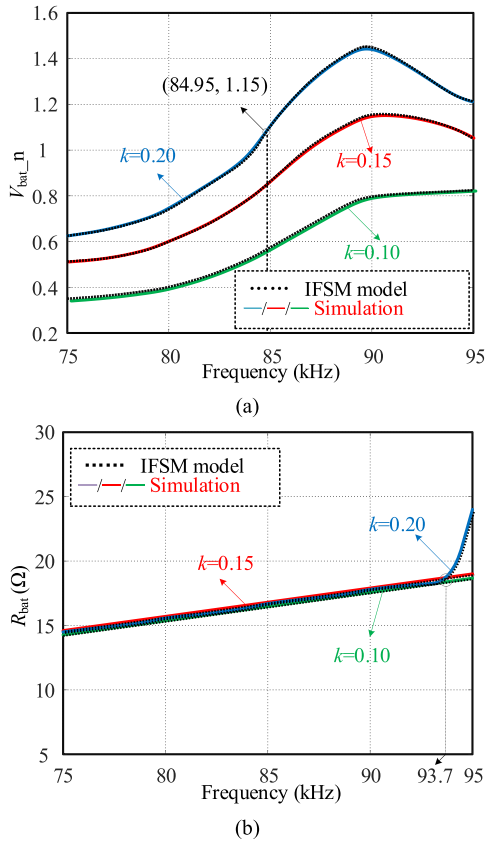

Fig. 17. Boundary voltage $V_{\mathrm{bat\_n}}$ and resistance R_{bat} with respect to operating frequency f_{s} when $V_{\mathrm{d}} = 400$ V. (a) $V_{\mathrm{bat\_n}}$. (b) R_{bat}.

than the initial values. In this article, Δk, ΔR_{bat}, and $\Delta\alpha$ are chosen as 0.001, 0.001 Ω, and −0.001 rad/s, respectively. To simplify the expression, the outputs of the flowchart are $\boldsymbol{M}_{i\_\mathrm{optim}}$ and $\boldsymbol{N}_{i\_\mathrm{optim}}$, which contain the parameters mutual inductance M and load resistance R_{bat}.

The characteristics of EV charging loads and equivalent resistance of the conventional 400-V battery packs are analyzed in [24]. Considering the parameters in this article, the range of load resistance R_{bat} is limited from 2 to 90 Ω, which can be treated as the entire load range. And the range of operating frequency is iterated from 75 to 95 kHz for a full demonstration. Based on the IFSM model described in Section III-C, the CCM/DCM boundaries with respect to load resistance R_{bat}, coupling coefficient k, and operating frequency f_{s} are analyzed. To intuitively analyze the relationship between the discontinuous boundary of the output current i_{s} of the compensation network and the battery voltage V_{bat}, R_{bat} is selected as the variable during the iteration process. When the R_{bat} and k are obtained in Fig. 15, it is easy to know the corresponding V_{bat} based on the IFSM model.

The results of boundary calculation are shown in Figs. 16 and 17, where $V_{\mathrm{bat\_n}}$ is defined as $V_{\mathrm{bat}}/400$. For uniform representation, regions above the curves are discontinuous zones, otherwise, regions below the curves are continuous zones. As shown in Fig. 16(a), the normalized boundary battery voltage is positively related to the coupling coefficient k in the full-power range when the load is 400-V or 800-V battery packs. Fig. 16(b) shows the equivalent boundary resistance R_{bat} of battery packs corresponding to the curves in Fig. 16(a). R_{bat} is almost constant when the coupling coefficient k varies from 0.1 to 0.3, indicating that the coupling coefficient k has little influence on the boundary load resistance.

Fig. 17 illustrates the boundary of normalized battery voltage $V_{\mathrm{bat\_n}}$ and equivalent boundary resistance R_{bat} with respect to the operating frequency f_{s}. As shown in Fig. 17(a), when the range of frequency f_{s} is from 79 to 90 kHz, which is required in international standard SAE J2954, the boundary voltage $V_{\mathrm{bat\_n}}$ increases with the operating frequency. What is more, when the coupling coefficients are 0.15 and 0.2, the point of inflection appears on the curve near the operating frequency $f_{\mathrm{s}} = 90$ kHz, indicating a significant decrease in the power transfer ability of the system. When coupling coefficient $k = 0.2$ and $f_{\mathrm{s}} = 84.95$ kHz, the boundary voltage is 460 V, which is consistent with the results in Fig. 16(a). When k decreases, the current i_{s} will enter the discontinuous region, otherwise, it will enter the continuous region.

It can be seen in Fig. 17(b) that there is a positive correlation between the equivalent boundary resistance R_{bat} and the operating frequency f_{s} when k is 0.1 and 0.15. However, when k is 0.2, the curve deviates from this trend at a frequency of 93.7 kHz. In correspondence with the curve of the boundary voltage variation, it is observed that for the parameters designed in this article, the operating frequency has surpassed the optimal range. Besides,

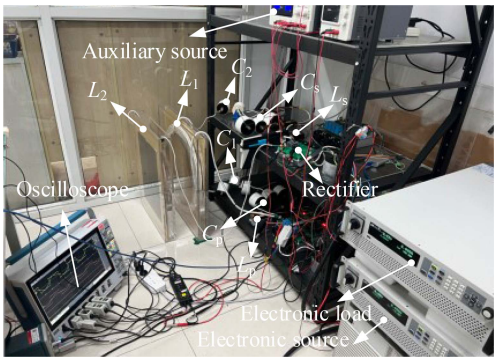

Fig. 18. Experimental prototype.

different from the relationship between R_{bat} and k, the boundary resistance R_{bat} varies from 14.5 to 24 Ω when the operating frequency f_{s} is from 75 to 95 kHz. The three curves overlap within the frequency range of 75–93.7 kHz, further confirming that the coefficient k has little effect on the CCM/DCM boundary of i_{s}.

C. Extension to Other Topologies

1) WPT Systems: The dual-side *LCC* WPT system for EV charging is taken as an example in this article to present the IFSM model. The establishment of the discrete-time model and boundary analysis process can be readily extended to other high-order compensation topologies in WPT systems. The differences that should be considered are as follows.

1) When the inverter operates with an asymmetric period or the load is a dc converter, additional operating states are introduced. Some simplifications in the model derivation process become ineffective in these cases, leading to an increase in model complexity.
2) When the dual-phase-shift control and triple-phase-shift control are adopted in the systems, constraints regarding the inner and outer phase-shift angles need to be incorporated. In addition, prior to boundary solving, it is necessary to analyze and determine the ZVS operation range to ensure that the boundary results comply with the system's ZVS operation. To improve the accuracy of the boundary calculation, the iteration step sizes should adapt to the operating frequency and time intervals during one operating period.
3) When studying the two-stage WPT systems [33], it is crucial to first select noncoupled independent state variables, and then model the entire cascade system. When the output capacitance is large enough, it is possible to decouple the two-stage topology. Thus, the accuracy obtained by modeling them separately also meets the requirements.

2) Nonisolated Converters: For a single low-order nonisolated dc–dc converters, such as buck, boost, and buck-boost converters, voltage-second and ampere-second balance principles are commonly used to derive the current expression. By leveraging the criterion of zero current, the operating states of the

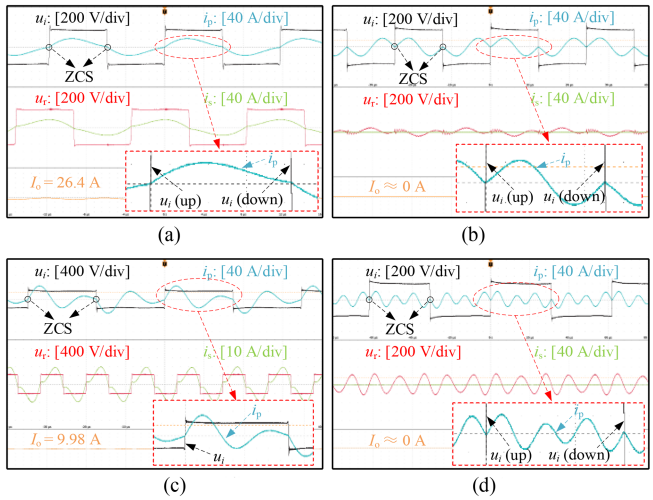

Fig. 19. Waveforms of points A, B, C, and D when $V_{\mathrm{in}} = V_{\mathrm{bat}} = 400$ V and $k = 0.2$. (a) $f_{\mathrm{A}} = 84.95$ kHz and time: 4 μs/div. (b) $f_{\mathrm{B}} = 39.46$ kHz and time: 10 μs/div. (c) $f_{\mathrm{C}} = 28.95$ kHz and time: 10 μs/div. (d) $f_{\mathrm{D}} = 16.02$ kHz and time: 20 μs/div.

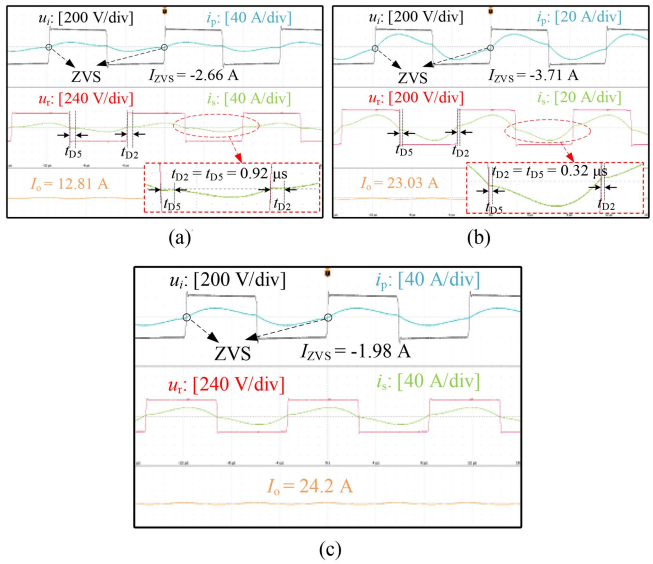

Fig. 20. Waveforms of the output voltage u_i and current i_{p} of the inverter and the input voltage u_{r} and current i_{s} of the rectifier when $V_{\mathrm{in}} = V_{\mathrm{bat}} = 400$ V and $f_{\mathrm{s}} = f_{\mathrm{A}} = 84.95$ kHz. (a) $k = 0.1$, DCM and time: 4 μs/div. (b) $k = 0.15$, DCM and time: 4 μs/div. (c) $k = 0.17$, CRM and time: 4 μs/div.

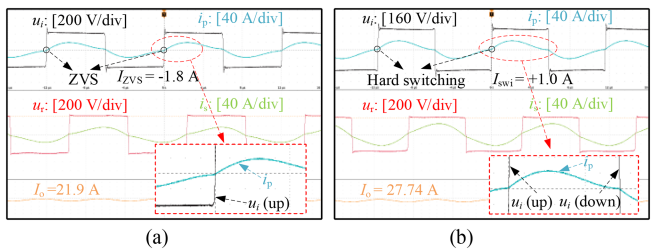

Fig. 21. Waveforms of the output voltage u_i and current i_{p} of the inverter and the input voltage u_{r} and current i_{s} of the rectifier when $V_{\mathrm{in}} = V_{\mathrm{bat}} = 400$ V, and $k = 0.2$. (a) $f_{\mathrm{s}} = 83$ kHz and time: 4 μs/div. (b) $f_{\mathrm{s}} = 86$ kHz and time: 4 μs/div.

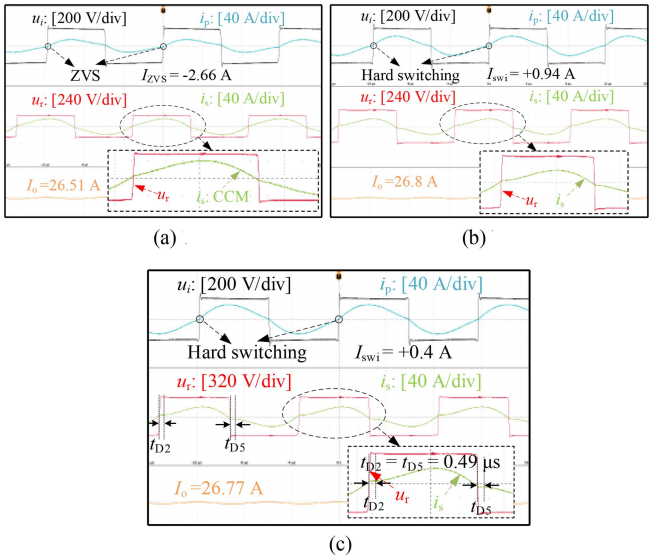

Fig. 22. Waveforms of the output voltage u_i and current i_p of the inverter and the input voltage u_r and current i_s of the rectifier when $V_{in} = 400$ V, $k = 0.2$ and $f_s = f_A = 84.95$ kHz. (a) $V_{bat\cdot n} = 0.75$, $R_{bat} = 11.32\ \Omega$, CCM and time: 4 μs/div. (b) $V_{bat\cdot n} = 1.15$, $R_{bat} = 17.16\ \Omega$, CRM and time: 4 μs/div. (c) $V_{bat\cdot n} = 1.25$, $R_{bat} = 18.68\ \Omega$, DCM and time: 4 μs/div.

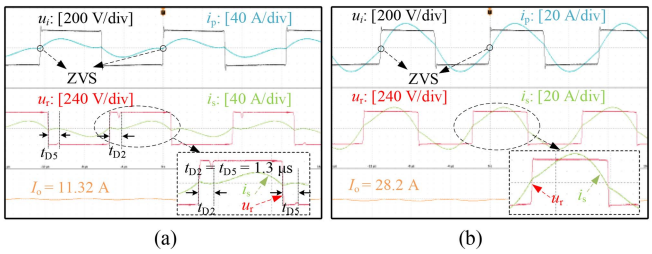

Fig. 23. Waveforms of the output voltage u_i and current i_p of the inverter and the input voltage u_r and current i_s of the rectifier when $V_{in} = 400$ V, $k = 0.2$ and $V_{bat\cdot n} = 1.15$. (a) $f_s = 80$ kHz, $R_{bat} = 40.64\ \Omega$, CCM, and time: 4 μs/div. (b) $f_s = 90$ kHz, $R_{bat} = 16.31\ \Omega$, CCM and time: 4 μs/div.

converter can be analyzed, facilitating the determination of the corresponding boundary parameter values. When state variables increase in nonisolated dc systems, leading to difficulties in solving, IFSM would be a preferable choice.

VI. Experimental Verification

To verify the IFSM model and theoretical analysis, as shown in Fig. 18, a dual-side *LCC*-compensated WPT prototype is built. Experimental parameters are given in Table III. The ZCS frequencies obtained in Section IV and boundary analysis results in Section V are verified in this section. Experimental waveforms are measured by an oscilloscope (Tektronix MSO58 8-BW-500). The inverter consists of eight SiC MOSFETs (C3M0021120Ks), and the rectifier consists of four diodes (STTH75S12Ws).

A. ZCS Points Verification

Fig. 19 shows the waveforms of the output voltage u_i and current i_p of the inverter, and the input voltage u_r and current i_s

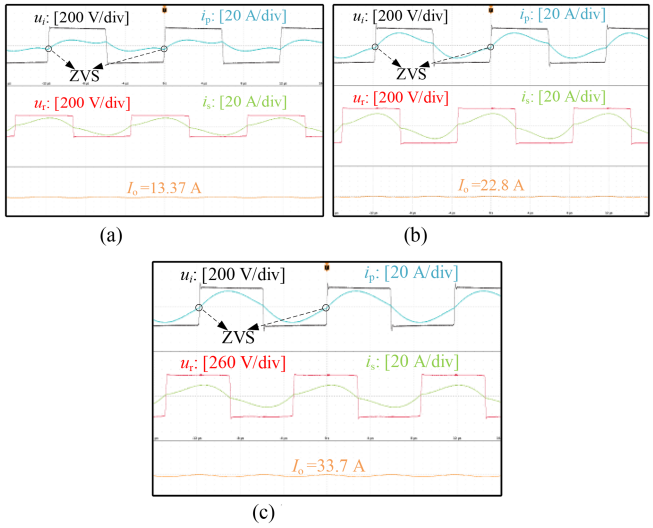

Fig. 24. Waveforms of the output voltage u_i and current i_p of the inverter and the input voltage u_r and current i_s of the rectifier when $V_{in} = 400$ V and $f_s = f_A = 84.95$ kHz. (a) $k = 0.1$, $V_{bat\cdot n} = 0.575$, $R_{bat} = 17.20\ \Omega$, CRM, and time: 4 μs/div. (b) $k = 0.15$, $V_{bat\cdot n} = 0.98$, $R_{bat} = 17.19\ \Omega$, CRM, and time: 4 μs/div. (c) $k = 0.25$, $V_{bat\cdot n} = 1.45$, $R_{bat} = 17.21\ \Omega$, CRM, and time: 4 μs/div.

of the rectifier when the inverter operates at different frequencies obtained in (31). The dc input voltage and the voltage of the battery packs are given as 400 V when $k = 0.2$. When $f = f_A$, f_B, f_C, and f_D, the experimental results of current i_p are highly consistent with the simulation waveforms. When the dual-side *LCC* compensated WPT system operates at frequencies f_A and f_C, the output current I_o is 26.4 A and 9.98 A. However, when the system operates at frequencies f_B and f_D, the output current is almost zero, which means that there is no power transferred to the load. Thus, f_B and f_D cannot be chosen as the operating frequency of the system.

Fig. 20 shows the waveforms of the compensation network when the operating frequency is fixed at $f_s = f_A = 84.95$ kHz. The exact ZCS frequency is 84.95 kHz when $V_{in} = V_{bat} = 400$ V and $k = 0.2$. It can be seen in Fig. 20(a) and (b) that when the coupling coefficient is 0.1 and 0.15, which is smaller than 0.2, the load will operate in DCM. The smaller the coupling coefficient k is, the longer the time in DCM is. And the inverter will operate in ZVS zones, the ZVS currents are -2.66 A and -3.17 A when $k = 0.1$ and 0.15, respectively. As shown in Fig. 14, a bifurcation will occur in the ZCS calculation results obtained by the traditional SM model and the IFSM model when $V_{in} = V_{bat} = 400$ V and $k = 0.17$, the experimental results confirm the accuracy of the model calculation. Besides, the waveforms presented in Figs. 19(a) and 20(a) and (b) have a good fit for the results obtained from the IFSM model and simulations shown in Fig. 9.

Fig. 21 shows the waveforms of the compensation network when k is fixed at 0.2 and $V_{in} = V_{bat} = 400$ V. When the operating frequency f_s is lower than the ZCS frequency f_A, the ZVS current of the MOSFETs is -1.8 A. However, when f_s is higher than f_A, the inverter will operate in a hard-switching zone. The results and analysis above also prove that the IFSM model has high accuracy when system parameters are given. Generally, to

TABLE VI
COMPARISON OF DIFFERENT MODELING METHODS

Literature	[12]	[13]	[14], [15]	[16], [17]	[22]	**This article**
Modeling methods	GSSA	EDF	CMT	PT	SM	**IFSM**
Discretization method	/	/	/	/	Yes	Yes
Studied topology	LCC-LCC	SS	SS	SS	Buck	LCC-LCC
Order of the model	17^{th} (High)	9^{th} (Medium)	4^{th} (Low)	4^{th} (Low)	2^{nd} (Low)	9^{th} (Medium)
Accuracy	<97%	Medium	>99%	Medium	<90%	>98%
ZCS calculation	YES	NO	NO	NO	YES (CCM)	YES (CCM and DCM)
Applicability	DC/AC input	AC input	DC input	DC input	DC–DC	DC–DC
Complexity for high-order systems	High	High	High	High	Low	Medium

reduce the switching losses, the ZVS is more important to the MOSFETs, and the ZCS is crucial to the IGBTs. The inverter consisting of MOSFETs is just used as an example to demonstrate the model analysis in this article.

B. CCM/DCM Boundary Verification

Fig. 22 shows the waveforms of the compensation network when the battery voltage changes. The boundary voltage $V_{\mathrm{bat\cdot n}}$ is 1.15 and the corresponding load resistance is 17.2 Ω. It can be seen in Fig. 22(a) that when $V_{\mathrm{bat\cdot n}} = 0.75$, which is below the boundary voltage, i_{s} is in CCM. However, as shown in Fig. 22(c) when the battery voltage is above the boundary voltage, i_{s} is in DCM. The boundary equivalent resistance of the battery packs presented in Fig. 22(b) is almost equal to the results shown in Fig. 16(b). What is more, when the battery voltage is above the ZCS voltage described in Fig. 19(a), the inverter will operate in the hard-switching zone again. The analysis above is also meaningful for the equivalent load resistance. The results shown in Fig. 22 also describe the characteristics of the CC output of the dual-side *LCC* compensation network.

Fig. 23 shows the waveforms of the compensation network when the operating frequency changes. The boundary voltage is 460 V when $f_{\mathrm{s}} = f_{\mathrm{A}} = 84.95$ kHz, the current becomes discontinuous when the operating frequency is lower than f_{A}, which is shown in Fig. 23(a). To ensure the load operates in CCM and reduces the THD of the load current of the WPT system, the proposed IFSM model can give the accurate boundary results as analyzed in Section V.

Fig. 24 shows the waveforms of the compensation network when the operating frequency f_{s} is fixed at f_{A} and the coupling coefficient k changes. The boundary voltages $V_{\mathrm{bat\cdot n}}$ are 0.575, 0.98, 1.15, and 1.45 when $k = 0.1$, $k = 0.15$, $k = 0.2$, and $k = 0.25$, obtained in Section V, respectively. According to the results measured in experimental waveforms, the boundary equivalent resistances R_{bat} are 17.20, 17.19, 17.16, and 17.21 Ω, which match well with the theoretical results shown in Figs. 16(b) and 17(b).

In Figs. 19(a), (b), and 22(c), different from the results of ideal case and simulations, the current i_{s} is not strictly equal to zero when the system operates in DCM mode. The deviation can be attributed to nonidealities in the components used in the practical experiments. The parasitic resistances and inductances introduce discrepancies from the theoretically anticipated behaviors. When the diode is in a nonconductive state, the interplay between parasitic parameters and compensation components gives rise to an oscillation circuit, resulting in a current bias.

Furthermore, the system operates in DCM for a short duration, which is much shorter than the operating period T_{s}, which presents a challenge in effectively counteracting the inertia of the circuit. Consequently, the system experiences minimal voltage distortion during these intervals. In fact, prolonged operation in DCM will lead to oscillations in the current waveform, characterized by zero crossings, accompanied by noticeable voltage distortion.

C. Comparison and Discussion

Table VI compares the performance of different methods in terms of modeling accuracy, model complexity, and applicability. Unlike methods in [30], [31], and [32], the development of the IFSM model in this article has clear discrete sampling points and can be adjusted according to the different operating states of the system. The difficulty in choosing the sampling step size is avoided. Besides, the analytical solutions can conveniently be obtained for high-order dc–dc systems. According to the experimental results presented in Section VI-A and B, the proposed model in this article has high accuracy and medium complexity. For high-frequency WPT systems where the ZCS and ZVS are important for reducing switching losses, the IFSM model is a better choice. Meanwhile, when the order of the studied system is too high, a discrete reduced-order model can also be developed based on the IFSM model, which will greatly reduce the analysis complexity.

VII. CONCLUSION

To improve the accuracy and the extendibility of the discrete-time model, an IFSM model is proposed in this article, which contains all information when the operating state of the system changes. Given the system parameters, the IFSM model can be used to calculate the possible ZCS points of the inverter and find the optimal one. Although only the input current of dual-side *LCC* is analyzed, the discrete-time model is still valid

if the load on the secondary side is a full-bridge inverter. The optimal ZCS operating frequency is strictly related to the load, and only the best operating frequency under certain conditions is calculated to prove the correctness of the IFSM model in this article. Furthermore, based on the IFSM model, the CCM/DCM boundary of the dual-side *LCC* output current in the full-power and full-frequency range is analyzed. The discrete-time model and calculation process can be extended to other WPT and dc–dc systems, especially for high-order systems, and any parameter can be chosen as a variable to analyze its influence on the boundary.

APPENDIX

The matrices of the IFSM model in CCM and DCM are given as follows:

$$\boldsymbol{N}_{\mathrm{C1}} = \left(\frac{1}{L_{\mathrm{p}}}\,0\,0\,0\,0\,0\,0\,0\,0\right)^{T} \tag{35}$$

$$\boldsymbol{N}_{\mathrm{D1}} = \left(-\frac{1}{L_{\mathrm{p}}}\,0\,0\,0\,0\,0\,0\,0\,0\right)^{T} \tag{36}$$

$$\boldsymbol{N}_{\mathrm{C1}} = \boldsymbol{N}_{\mathrm{C2}} = -\boldsymbol{N}_{\mathrm{C3}} = -\boldsymbol{N}_{\mathrm{C4}} \tag{37}$$

$$\boldsymbol{N}_{\mathrm{D1}} = \boldsymbol{N}_{\mathrm{D2}} = \boldsymbol{N}_{\mathrm{D3}} = -\boldsymbol{N}_{\mathrm{D4}} = -\boldsymbol{N}_{\mathrm{D5}} = -\boldsymbol{N}_{\mathrm{D6}} \tag{38}$$

$$\boldsymbol{M}_{\mathrm{D1}} = \boldsymbol{M}_{\mathrm{D3}} = \boldsymbol{M}_{\mathrm{D4}} = \boldsymbol{M}_{\mathrm{D6}} = \boldsymbol{M}_{\mathrm{C1}} \tag{39}$$

$$\boldsymbol{M}_{\mathrm{C1}} = \boldsymbol{M}_{\mathrm{C2}} = \boldsymbol{M}_{\mathrm{C3}} = \boldsymbol{M}_{\mathrm{C4}}$$

$$= \begin{pmatrix} 0 & -\frac{1}{L_{\mathrm{p}}} & 0 & 0 & 0 & 0 & 0 & 0 & 0 \\ \frac{1}{C_{\mathrm{p}}} & 0 & 0 & -\frac{1}{C_{\mathrm{p}}} & 0 & 0 & 0 & 0 & 0 \\ 0 & 0 & 0 & \frac{1}{C_1} & 0 & 0 & 0 & 0 & 0 \\ 0 & \frac{L_2}{\Delta} & -\frac{L_2}{\Delta} & 0 & 0 & \frac{M}{\Delta} & -\frac{M}{\Delta} & 0 & 0 \\ 0 & -\frac{M}{\Delta} & \frac{M}{\Delta} & 0 & 0 & -\frac{L_1}{\Delta} & \frac{L_1}{\Delta} & 0 & 0 \\ 0 & 0 & 0 & 0 & \frac{1}{C_2} & 0 & 0 & 0 & 0 \\ 0 & 0 & 0 & 0 & -\frac{1}{C_{\mathrm{s}}} & 0 & 0 & \frac{1}{C_{\mathrm{s}}} & 0 \\ 0 & 0 & 0 & 0 & 0 & 0 & -\frac{1}{L_{\mathrm{s}}} & 0 & \frac{1}{L_{\mathrm{s}}} \\ 0 & 0 & 0 & 0 & 0 & 0 & 0 & -\frac{1}{C_{\mathrm{o}}} & -\frac{1}{R_{\mathrm{bat}} C_{\mathrm{o}}} \end{pmatrix} \tag{40}$$

$$\boldsymbol{M}_{\mathrm{D2}} = \boldsymbol{M}_{\mathrm{D5}}$$

$$= \begin{pmatrix} 0 & -\frac{1}{L_{\mathrm{p}}} & 0 & 0 & 0 & 0 & 0 & 0 & 0 \\ \frac{1}{C_{\mathrm{p}}} & 0 & 0 & -\frac{1}{C_{\mathrm{p}}} & 0 & 0 & 0 & 0 & 0 \\ 0 & 0 & 0 & \frac{1}{C_1} & 0 & 0 & 0 & 0 & 0 \\ 0 & \frac{L_2}{\Delta} & -\frac{L_2}{\Delta} & 0 & 0 & -\frac{M}{\Delta} & -\frac{M}{\Delta} & 0 & 0 \\ 0 & -\frac{M}{\Delta} & \frac{M}{\Delta} & 0 & 0 & \frac{L_1}{\Delta} & \frac{L_1}{\Delta} & 0 & 0 \\ 0 & 0 & 0 & 0 & \frac{1}{C_2} & 0 & 0 & 0 & 0 \\ 0 & 0 & 0 & 0 & \frac{1}{C_{\mathrm{s}}} & 0 & 0 & 0 & 0 \\ 0 & 0 & 0 & 0 & 0 & 0 & 0 & 0 & 0 \\ 0 & 0 & 0 & 0 & 0 & 0 & 0 & 0 & -\frac{1}{R_{\mathrm{bat}} C_{\mathrm{o}}} \end{pmatrix}. \tag{41}$$

REFERENCES

[1] Y. Chen, H. Zhang, C.-S. Shin, C.-H. Jo, S.-J. Park, and D.-H. Kim, "An efficiency optimization-based asymmetric tuning method of double-sided LCC compensated WPT system for electric vehicles," *IEEE Trans. Power Electron.*, vol. 35, no. 11, pp. 11475–11487, Nov. 2020.

[2] X. Liu, T. Wang, F. Gao, M. M. Khan, X. Yang, and D. J. Rogers, "A resonant inductor integrated-transformer-based receiver for wireless power transfer systems," *IEEE Trans. Ind. Electron.*, vol. 70, no. 4, pp. 3616–3626, Apr. 2023.

[3] W. Li, H. Zhao, J. Deng, S. Li, and C. C. Mi, "Comparison study on SS and double-sided LCC compensation topologies for EV/PHEV wireless chargers," *IEEE Trans. Veh. Technol.*, vol. 65, no. 6, pp. 4429–4439, Jun. 2016.

[4] P. Brick, "48V battery pack-lithium iron-phosphate (LiFePO4) 25Ah," 2017. [Online]. Available: https://www.powertechsystems.eu/wpcontent/uploads/sites/2/2017/07/PowerBrick_25Ah_48V_EN.pdf

[5] T. Ma, C. Jiang, J. Xiang, X. Wang, K. T. Chau, and T. Long, "Modeling and analysis of wireless power transfer system via unified full-load discrete-time model," *IEEE Trans. Ind. Electron.*, vol. 70, no. 6, pp. 5626–5636, Jun. 2023.

[6] W. Shi, J. Dong, T. B. Soeiro, and P. Bauer, "Integrated solution for electric vehicle and foreign object detection in the application of dynamic inductive power transfer," *IEEE Trans. Veh. Technol.*, vol. 70, no. 11, pp. 11365–11377, Nov. 2021.

[7] Y. Li, J. Hu, F. Chen, Z. Li, Z. He, and R. Mai, "Dual-phase-shift control scheme with current-stress and efficiency optimization for wireless power transfer systems," *IEEE Trans. Circuits Syst. I, Regular Papers*, vol. 65, no. 9, pp. 3110–3121, Sep. 2018.

[8] A. Babaki, S. Vaez-Zadeh, A. Zakerian, and G. A. Covic, "Variable-frequency retuned WPT system for power transfer and efficiency improvement in dynamic EV charging with fixed voltage characteristic," *IEEE Trans. Energy Convers.*, vol. 36, no. 3, pp. 2141–2151, Sep. 2021.

[9] T.-J. Liang, K.-H. Chen, and J.-F. Chen, "Primary side control for flyback converter operating in DCM and CCM," *IEEE Trans. Power Electron.*, vol. 33, no. 4, pp. 3604–3612, Apr. 2018.

[10] S. Li, W. Li, J. Deng, T. D. Nguyen, and C. C. Mi, "A double-sided LCC compensation network and its tuning method for wireless power transfer," *IEEE Trans. Veh. Technol.*, vol. 64, no. 6, pp. 2261–2273, Jun. 2015.

[11] C. Wang, Z. Wang, Q. Wu, and H. Xin, "An improved impedance/admittance analysis method considering collector subsystem transformation in converter-integrated power systems," *IEEE Trans. Power Syst.*, vol. 36, no. 6, pp. 5963–5966, Nov. 2021.

[12] H. Li, J. Xu, F. Gao, Y. Zhang, X. Yang, and H. Tang, "Duty cycle control strategy for dual-side LCC resonant converter in wireless power transfer systems," *IEEE Trans. Transp. Electrific.*, vol. 8, no. 2, pp. 1944–1955, Jun. 2022.

[13] Z. U. Zahid et al., "Modeling and control of series–series compensated inductive power transfer system," *IEEE J. Emerg. Sel. Topics Power Electron.*, vol. 3, no. 1, pp. 111–123, Mar. 2015.

[14] A. Kurs et al., "Wireless power transfer via strongly coupled magnetic resonances," *Sci. Exp.*, vol. 317, pp. 83–86, Jul. 2007.

[15] Z. Wei and B. Zhang, "Transmission range extension of PT-symmetry-based wireless power transfer system," *IEEE Trans. Power Electron.*, vol. 36, no. 10, pp. 11135–11147, Oct. 2021.

[16] S. Assawaworrarit, X. Yu, and S. Fan, "Robust wireless power transfer using a nonlinear parity-time-symmetric circuit," *Nature*, vol. 546, no. 7658, pp. 387–390, 2017.

[17] J. Zhou, B. Zhang, W. Xiao, D. Qiu, and Y. Chen, "Nonlinear parity-time-symmetric model for constant efficiency wireless power transfer: Application to a drone-in-flight wireless charging platform," *IEEE Trans. Ind. Electron.*, vol. 66, no. 5, pp. 4097–4107, May 2019.

[18] S. Cochran and D. Costinett, "Discrete time synchronization modeling for active rectifiers in wireless power transfer systems," in *Proc. 20th Workshop Control Model. Power Electron.*, 2019, pp. 1–8.

[19] C. Cheng, F. Xie, B. Zhang, D. Qiu, W. Xiao, and H. Ji, "Modeling and nonlinear dynamic analysis of cascaded DC–DC Converter systems based on simplified discrete mapping," *IEEE Trans. Ind. Electron.*, vol. 70, no. 6, pp. 5830–5839, Jun. 2023.

[20] X. Hu et al., "Discrete time modeling of wireless power transfer system using LCC compensation topology," in *Proc. 10th Int. Conf. Power Electron. ECCE Asia*, 2019, pp. 968–973.

[21] S. Cochran and D. Costinett, "Dual-loop frequency synchronization and load regulation using a discrete time model for a 7-level switched capacitor WPT rectifier," in *Proc. IEEE 21st Workshop Control Model. Power Electron.*, 2020, pp. 1–8.

[22] S. Maity, D. Tripathy, T. K. Bhattacharya, and S. Banerjee, "Bifurcation analysis of PWM-1 voltage-mode-controlled buck converter using the exact discrete model," *IEEE Trans. Circuits Syst. I, Regular Papers*, vol. 54, no. 5, pp. 1120–1130, May 2007.

[23] X. Liu, C. Xia, X. Han, Z. Wu, and Z. Liao, "Simultaneous wireless power and information transmission based on harmonic characteristic of soft-switching inverter," *IEEE Trans. Ind. Electron.*, vol. 69, no. 6, pp. 6090–6100, Jun. 2022.
[24] A. M. A. Haidar and K. M. Muttaqi, "Behavioral characterization of electric vehicle charging loads in a distribution power grid through modeling of battery chargers," *IEEE Trans. Ind. Appl.*, vol. 52, no. 1, pp. 483–492, Jan./Feb. 2016.
[25] *Wireless Power Transfer for Light-Duty Plug-in/Electric Vehicles and Alignment Methodology*, International Standard SAE J2954, 2019. [Online]. Available: https://www.sae.org/standards/content/j2954_201904
[26] S. Li, P. Zhao, C. Gu, J. Li, D. Huo, and S. Cheng, "Aging mitigation for battery energy storage system in electric vehicles," *IEEE Trans. Smart Grid*, vol. 14, no. 3, pp. 2152–2163, May 2023.
[27] K. R. Kothapalli, M. R. Ramteke, and H. M. Suryawanshi, "ZVS–ZCS high step-up/step-down isolated bidirectional DC–DC converter for DC microgrid," *IEEE Trans. Power Electron.*, vol. 38, no. 6, pp. 7733–7745, Jun. 2023.
[28] N. K. Reddi, M. R. Ramteke, H. M. Suryawanshi, K. Kothapalli, and S. P. Gawande, "An isolated multi-input ZCS DC–DC front-end-converter based multilevel inverter for the integration of renewable energy sources," *IEEE Trans. Ind. Appl.*, vol. 54, no. 1, pp. 494–504, Jan./Feb. 2018.
[29] N. Fu, J. Deng, Z. Wang, W. Wang, and S. Wang, "A hybrid mode control strategy for LCC–LCC compensated WPT system with wide ZVS operation," *IEEE Trans. Power Electron.*, vol. 37, no. 2, pp. 2449–2460, Feb. 2022.
[30] H. Ji, F. Xie, Y. Chen, and B. Zhang, "Small-step discretization method for modeling and stability analysis of cascaded DC–DC converters with considering different switching frequencies," *IEEE Trans. Power Electron.*, vol. 37, no. 8, pp. 8855–8872, Aug. 2022.
[31] X. Li, X. Ruan, Q. Jin, M. Sha, and C. K. Tse, "Approximate discrete-time modeling of DC–DC converters with consideration of the effects of pulse width modulation," *IEEE Trans. Power Electron.*, vol. 33, no. 8, pp. 7071–7082, Aug. 2018.
[32] M. T. Iqbal and A. I. Maswood, "An explicit discrete-time large- and small-signal modeling of the dual active bridge DC–DC converter based on the time scale methodology," *IEEE J. Emerg. Sel. Topics Power Electron.*, vol. 2, no. 4, pp. 545–555, Oct. 2021.
[33] F. Wu, Y. Wei, J. Su, K. Zhao, and H. Liu, "Dual-side closed-loop control, stability analysis, and parameter design of two-stage LCC-LCC WPT," *IEEE J. Emerg. Sel. Topics Power Electron.*, vol. 12, no. 1, pp. 305–315, Feb. 2024.

Kai He (Student Member, IEEE) received the B.S. degree in electrical engineering from East China University of Science and Technology, Shanghai, China, in 2021. He is currently working toward the Ph.D. degree in electrical engineering with Shanghai Jiao Tong University, Shanghai, China.

His research interests include modeling and control of high-order WPT systems.

Xin Liu (Member, IEEE) received the B.S. degree in electrical engineering from Wuhan University, Wuhan, China, in 2015, and the Ph.D. degree in electrical engineering from Shanghai Jiao Tong University, Shanghai, China, in 2019.

From 2019 to 2021, he worked with Huawei Technologies Company Ltd. From 2021 to 2023, he has been with the Department of Electrical Engineering, Shanghai Jiao Tong University as a Postdoctoral Researcher. In September 2023, he joined Shenzhen Institute for Advanced Study, University of Electronic Science and Technology of China as an Associate Researcher. His current research interests include wireless power transfer and solid-state transformers.

Fei Gao (Member, IEEE) received the Ph.D. degree in electrical engineering from the Power Electronics, Machines, and Control (PEMC) Research Group, University of Nottingham, Nottingham, U.K., in 2016.

From 2010 to 2012, he worked with Jiangsu Electric Power Research Institute, Nanjing, State Grid Corporation of China. From 2016 to 2019, he was with the Department of Engineering Science, University of Oxford, Oxford, U.K., as a Postdoctoral Researcher. In 2019, he joined Shanghai Jiao Tong University as an Associate Professor. His current research interests include modeling, control, power management, and stability of microgrids and more electric transportation systems.

Dr. Gao was the recipient of the European Union Clean Sky Best PhD Award in 2017 and IET Control & Automation Runner Up Ph.D. Award in 2018.

Xijun Yang (Member, IEEE) received the Ph.D. degree in control engineering from Shanghai University, Shanghai, China, in 2002.

From 1992 to 1995, he worked as an Electrical Engineer with Handan Institute of Coal Mine Design and Research, Hebei, China. From 2013 to 2014, he worked as a guest Associate Professor with the Department of Energy Technology, Aalborg University, Aalborg, Denmark. From 2004 to 2013 and since 2014, he has been working with the Department of Electrical Engineering, Shanghai Jiao Tong University, Shanghai, China, as an Associate Professor. His current research interests include wireless power transfer, power conversion, and solid-state transformers.

Zhengshun Cheng received the Bachelor's and Master's degrees in ocean engineering from Shanghai Jiao Tong University (SJTU), Shanghai, China, in 2013 and 2010, respectively, and the Ph.D. degree in marine technology from Norwegian University of Science and Technology (NTNU), Trondheim, Norway, in 2016.

He has been an Associate Professor with the School of Ocean and Civil Engineering, SJTU, since 2019. Prior to this, he was a Postdoctoral Researcher with the Department of Marine Technology, NTNU. His research interests include coupled and stochastic dynamics of marine structures, offshore wind technology, marine renewable energy, etc.

Dr. Cheng was the recipient of the Moan-Faltinsen Best Paper Award in 2017 and OMAE Conference Best Paper Award in 2023.

Dong Liu (Senior Member, IEEE) received the B.S. and M.S. degrees in electrical engineering from Sichuan University, China, in 1989 and 1994, respectively, and the Ph.D. degree in electrical engineering from Southeast University, China, in 1997.

He is currently a Full Professor with the Department of Electrical Engineering, Shanghai Jiao Tong University, Shanghai, China. His research interests include smart grids and cyber-physical systems for power grids.